Journal of Low Temperature Physics, Vol. 93, Nos. 1/2, 1993

Second Sound Very Near T_λ

Lori S. Goldner,* Norbert Mulders,† and Guenter Ahlers

Department of Physics and Center for Nonlinear Science, University of California, Santa Barbara, California 93106

(Received May 24, 1993)

The results of an experimental investigation of the evolution of planar, nonlinear, second-sound pulses in superfluid ^4He, to within 650 nK of the λ-transition, are presented. A new method for extracting the second-sound velocity and damping is demonstrated. As predicted from two-fluid hydrodynamics, the pulses are well modeled by the solutions of Burgers' equation. The second-sound velocity (u_{20}) and damping (D_2) are extracted from fits of the model to the data. Damping data are obtained in this fashion to 3×10^{-7} in reduced temperature at saturated vapor pressure; nearly two decades closer to T_λ then any previous measurements. The superfluid density is extracted from the u_{20} measurements and the critical exponent, ζ, is determined. A study of very large amplitude pulses near T_λ is also presented. These pulses extend well beyond the range of validity of Burgers' equation. The amplitude of the shock that forms at the trailing edge of the pulse is observed to saturate as a function of heater power and then decrease suddenly, as has been previously observed away from T_λ. However, the pulse shapes are quite different from any previously observed.

1. INTRODUCTION

The behavior of ^4He very near the λ-transition has long been of interest in the study of critical phenomena. A combination of properties renders it an ideal choice for this purpose; the superfluid transition occurs along a critical line, so that a simple change of pressure provides a test of universality; as a liquid, helium is strain-free, and as a cryogenic liquid, it is also easily purified. Furthermore, the effects of gravity, problematic in

*Present address: National Institute of Standards and Technology, Bldg 221 Room A167, Gaithersburg, MD 20899.

†Present address: Department of Physics, Pennsylvania State University, University Park, PA 16802.

0022-2291/93/1000-0131$07.00/0

the study of liquid-gas and binary-mixture critical points, are quite small in helium.

The unique hydrodynamics of the superfluid state provides several interesting probes of the critical region. The phenomenon of second sound (entropy waves) has proven particularly useful. The superfluid fraction, ρ_s/ρ, can be extracted from the velocity of second sound. Since second sound can be detected extremely close to T_λ, second-sound velocity measurements have provided the most accurate and complete data on ρ_s/ρ to date.[1,2] From ρ_s/ρ the exponent ζ can be determined and the predictions of static renormalization group (RG) theory tested. From measurements of second-sound damping, the predictions of the dynamic RG theory can be tested.

Sufficiently near the λ-transition, nonlinear effects dominate the behavior of second sound. This complicates considerably the measurement of the second-sound velocity and damping, and requires that we consider at least the lowest order nonlinear terms in the analysis of the hydrodynamic equations. In a previous paper,[3] we showed that such a treatment describes well the evolution of nonlinear second-sound pulses for reduced temperatures $t \equiv 1 - T/T_\lambda$ as small as 10^{-3}. Here we show that, in fact, this analysis works well even for t near 3×10^{-7}, and that our understanding of weakly nonlinear second sound is therefore sufficient to allow us to measure the superfluid fraction and second-sound damping very near T_λ.

Second sound has also been used extensively as a probe of two-fluid hydrodynamics itself, and, more recently, of the apparent "breakdown" of two-fluid hydrodynamics (see for example Ref. 4 or 5) or of vortex dynamics.[5–16] In the present work, very large amplitude second-sound pulses very near T_λ were studied, and several new features are reported.

In Sec. 2 of this paper, the experiment is described. Second-sound pulse evolution was probed for $3 \times 10^{-7} \leqslant t \leqslant 10^{-2}$ for ^{4}He at vapor pressure. The model is reviewed in Sec. 3, with an emphasis on possible pitfalls very near the transition. In Section 4 the data for small amplitude pulses are discussed and the second-sound velocity and damping measurements are presented. Sections 5 and 6 contain discussions of the results for second-sound damping and superfluid fraction, respectively. Finally, in Sec. 7, the data involving large amplitude pulses are presented.

Part of the work presented in this paper is based on the Ph.D. Thesis of one of us (LSG). Additional details not covered in this paper may be found in that thesis.[17]

2. THE EXPERIMENT

2.1. The Cryostat

The cryostat used in these studies, a modified version of one described elsewhere,[18] is shown schematically in Fig. 1. The cryostat had three separate stages or platforms inside a vacuum can that was submersed in liquid ^{4}He; the refrigerator platform (a), the isothermal platform (b), and the cell platform (c). A continuously-operating pumped ^{4}He refrigerator[19] (not shown) was located on (a), which was typically regulated to milli-

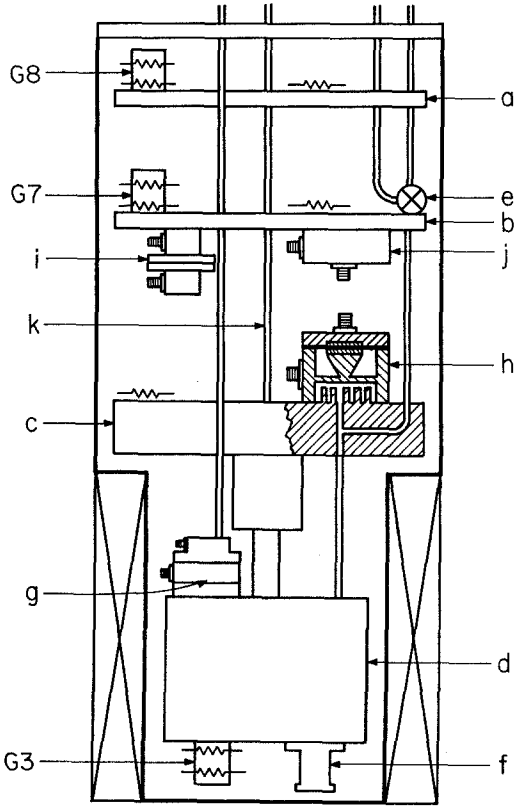

Fig. 1. The cryostat schematic. The refrigerator (a), isothermal stage (b), cell platform (c), cell (d), cold valve (e), T_λ-device (f), melting pressure thermometer (MPT) (g), pressure gauge (h), MPT reference capacitor (i), pressure gauge reference capacitor (j), and heatleak capillary (k) are shown. G3, G7 and G8 are germanium thermometers and reference resistors. Each stage also has a 5.1 kΩ heater.

Kelvin stability near 1.55 K. The isothermal platform was regulated to a stability of about 1 μK near 1.82 K with germanium thermometry, described below. On this thermally stable environment were located the reference capacitors (i, j) for a ^{4}He melting pressure thermometer[20] (g) and the pressure gauge (h), respectively. The pressure gauge was not extensively used in the work at vapor-pressure described here, but could be used in conjunction with a hot volume (not shown) to regulate the cell pressure to 0.1 μbar at 29 bar.[18] The melting pressure thermometer (g) could be used to regulate the cell (d) and cell platform to a stability of about 1 nK, as described briefly below and in Ref. 20. The cell and the cell reservoir were connected by 10 cm of a heavy stainless steel capillary (0.051 cm o.d.). A superconducting magnet, custom designed by American Magnetics[21] for very uniform fields over large horizontal areas, was used to bias the superconducting thin-film bolometers as described in Ref. 3. The magnet was located outside the can in the ^{4}He bath space.

Each platform had at least one previously calibrated germanium thermometer with a matching wire-wound reference resistor, and a 5.1 kΩ heater for use in temperature control and measurement. These thermometers were used in a five wire bridge-and-controller arrangement.[22] Manganin wires were used for all resistive thermometry and temperature control.

The cell is shown in Fig. 2. It was used and described previously,[3] and is shown here in somewhat more detail and drawn to scale. The working region of the cell (k) was defined on the top and bottom by two pyrex plates (bolometer and heater substrates), and on the sides by a copper spacer (j). The cavity (k) was square and quite short, $3.18 \times 3.18 \times 0.1203$ cm^3. The second-sound generator, a chromium heater that exactly spanned the lateral dimensions of the cell (3.18×3.18 cm^2), was located on the inner surface of the bottom Pyrex plate. It faced the second-sound detector, a small superconducting thin-film bolometer, centered on the inner surface of the top Pyrex plate. Inside the cell, two pairs of copper wires were attached to the heater, so that four-wire measurements of the heater voltage and resistance were possible. The wires were soldered to gold film electrodes on the heater, and were connected *via* two Microtech hermetically sealed feedthroughs (h) to cryogenic shielded twisted pairs. In a similar way, the bolometer was connected to a single shielded twisted pair.

2.2. Thermometry

The ^{4}He melting pressure thermometer[20] (MPT) utilizes the temperature dependence of the melting pressure and is capable of resolving temperature changes near T_λ of 1 nK. A Straty-Adams style strain gauge[23]

was used to convert changes in pressure to changes in capacitance. A three-wire coaxial bridge[20] was used to measure the capacitance of the gauge, and an LR-130 temperature controller regulated the temperature to an rms noise level near 1 nK. The MPT and reference capacitor used in the bridge are shown in Fig. 1.

The accuracy of the temperature measurement was determined by the accuracy with which a fixed point, in this case T_λ at saturated vapor pressure, could be measured. A small thermal conductivity cell (called "the T_λ-device") attached to the bottom of the sample cell (Fig. 2) could be used to measure the onset of thermal resistance in the superfluid, thereby determining T_λ to an accuracy of about 5 nK. Since the λ-point is shifted under gravity by $1.273 \pm 0.013\ \mu$K per cm of helium[24–26] (at vapor pressure), T_λ at the T_λ-device is shifted by about $5\ \mu$K from T_λ at the center of the cell (the bottom of the T_λ-device is nearly 4 cm from the center of the cell). The

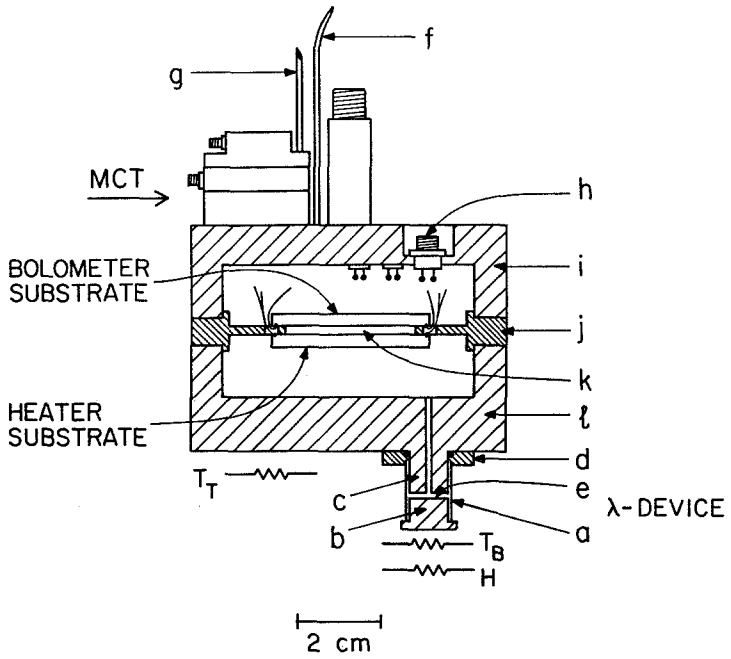

Fig. 2. The sample cell, drawn to scale. The T_λ-device (a–d) consists of a stainless steel sidewall (a), two copper end pieces (b, c), a copper flange (d), a helium filled gap (e), a pair of carbon thermometers (T_T and T_b) and a metal film heater resistor (H), nominal value 5.3 kΩ at 300 K. Also shown are the cell fill capillary (f), the MPT fill capillary (g), the electrical feedthrough (h), the cell top cap (i), body or spacer (j) and bottom cap (1), and the second sound cell cavity (k).

bolometer could also be used to measure T_λ to a precision of 1 nK and an accuracy of 20 nK by observing the change in self-heating of the device at the transition. Thus the T_λ-device could be "calibrated" against the bolometer to an accuracy of 20 nK, a somewhat better result than if we relied on the accuracy of the previously measured gravity shift and our knowledge of the cell length. Conversely, our measurement of T_λ at the two points in the cell gave a value for the shift in T_λ under gravity that agrees with previous measurements to within the combined errors. The precision of our final measurement of T_λ was 5 nK and the accuracy about 20 nK.

2.3. Electronics

The heater current leads were driven by a Wavetek model 178 programmable waveform synthesizer. The output of the synthesizer was run through a FET switch that was used for protection purposes. The operation of the FET switch, and the triggering of pulses at the synthesizer, was controlled by the timer outputs of a Tecmar Labmaster board (model number 020009) in an IBM model XT computer. The timers were run through optical isolators to avoid ground problems. The heater voltage leads were connected directly to the input of a digitizer (a Nicolet model 12/70 signal processor, eight bits, 20 MHz). The synchronous output of the synthesizer was used, through a pulse transformer, to trigger the digitizer. In this manner the voltage across the heater was recorded. The four leads also allowed for an accurate measurement of the heater resistance (typically 116.7 Ω) so that the power input at the heater was well known.

The bolometer was biased at constant current with a simple current supply, consisting of one or more batteries, a good 10 V regulator, and metal-film resistor in series. The voltage across a reference resistor ($R_{\text{ref}} = 10\ \text{k}\Omega$) could be monitored so that the current through the device was accurately known. The ac voltage output was monitored with a Princeton Applied Research model 118 preamplifier, typically used in differential mode, plugged into a model 114 filtering box. The bias source and the preamplifier were located as close as possible to the top of the cryostat in order to reduce lead capacitance, and therefore increase the frequency response of the circuit. The bolometer was typically operated at a resistance of about 200 Ω, set by the magnet bias, for the same reason (it was useable between 100 and about 4000 Ω). Both the current through the device and the dc voltage across it (V_b) were recorded in between data taking, thereby providing a resistance measurement. The cryogenic cables to the bolometer were all either copper plated or superconducting, so that the voltage drop across the leads was negligible. Static calibrations of the bolometer (resistance vs. temperature) were performed every time the bias current or

field was changed. Dynamic calibrations, using the second-sound amplitude calculated from the power of a pulse launched at the heater, confirmed the static calibration to better than 3%.

The bolometer was operated near two different current biases, a factor of 12 apart in power dissipation. Typical dissipation for the higher current bias (47.6 μA) was about 0.52 μW. For the lower bias (9.94 μA), the dissipation was near 0.043 μW. The sensitivity of the device was approximately 16 kΩ/K for the higher bias level and 45 kΩ/K for the lower.

2.4. Procedure

The cell was filled with ultra pure ^{4}He, containing less than 0.5×10^{-9} parts ^{3}He by mass,[27] to a pressure of 600 torr at 3.2 K. Cooled to 2.172 K, the cell was at vapor pressure with the liquid level in the cell reservoir above the working region.

The temperature at the cell platform was controlled differently depending on the distance from T_λ. For $t < 5.5 \times 10^{-4}$, the MPT was used to control temperature. For $t > 5.5 \times 10^{-4}$, a germanium thermometer was used and the distance to T_λ was known to about 1 μK. Reduced temperatures were always measured with respect to T_λ at the *center* of the cell.

A voltage pulse, consisting of a single cycle of a haversine, was applied at the heater and launched a second-sound pulse into the helium. This pulse propagated across the cell and was detected each time it reflected off of the surface containing the bolometer. The geometry of the cell was such that, at the bolometer, the first six pulse echoes were free from effects from the edge of the heater or reflections of second sound off the wall; i.e., the pulse remained quite planar until after its sixth arrival at the bolometer. The recorded data always represent the bolometer temperature as a function of time, and generally consist of the first six arrivals of the pulse at the detector. Due to the reflection at the surface of the bolometer, the temperature amplitude recorded at the bolometer is roughly a factor of two larger than the amplitude of the second sound as it propagates across the cell. A detailed discussion of substrate modeling and boundary conditions is given in Ref. 3.

Signal averaging of up to 20,000 pulse sequences was used to increase the signal-to-noise ratio. Heater pulses were launched every 1 to 4 seconds. The time interval was chosen to be long enough to allow the previous pulse to completely decay away. The bandwidth of the bolmometer circuitry was also carefully chosen to limit noise while not distorting the pulses,[3] and in this fashion rms noise levels as low as 2 or 3 nK could be achieved (see for example Fig. 8).

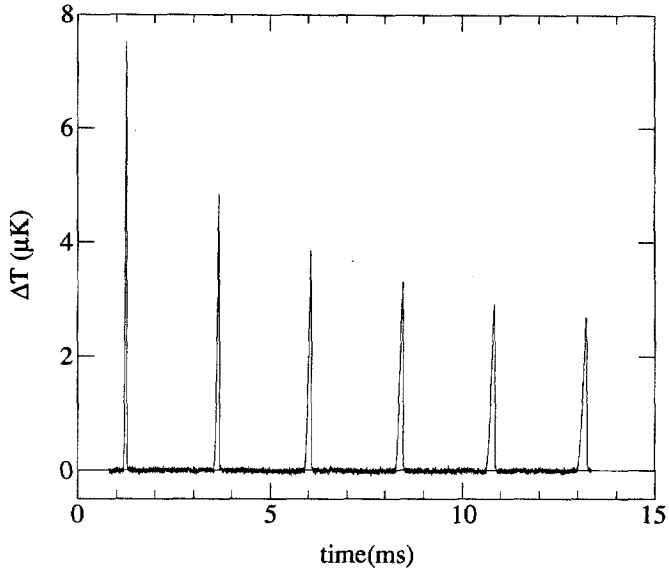

Fig. 3. A typical data set. Here $t = 5.0141 \times 10^{-5}$ and the rms noise is about 30 nK. This is the first 6 arrivals of a second sound pulse at the bolometer. The left hand scale is the temperature change measured at the bolometer.

A typical data set is shown in Fig. 3. Here 2000 pulse sequences, one every 1.7 s, have been averaged to achieved an rms noise level of about 30 nK. The reduced temperature was 5.014×10^{-5}. The temperature change at the bolometer as a funuction of time is shown.

3. ANALYSIS

3.1. Overview of the Model

The model used to extract u_{20} and D_2 in these experiments is identical to that described in Ref. 3. Here we discuss the use of this model near T_λ.

The method used to model the data uses Burgers' equation

$$\frac{\partial v_n}{\partial t} = \frac{D_2}{2}\frac{\partial^2 v_n}{\partial x^2} + (u_{20} + \alpha_2 v_n)\frac{\partial v_n}{\partial x} \tag{1}$$

to describe the propagation of second sound.[28-30] Here v_n is the normal fluid velocity, D_2 is the second-sound damping, u_{20} is the velocity of linear second sound

$$u_{20}^2 = \sigma^2 \frac{\rho_s T}{\rho_n C_p} \tag{2}$$

and α_2 is the Khalatnikov nonlinear coefficient[31]

$$\alpha_2 = \frac{\sigma T}{C_p}\frac{\partial}{\partial T}\ln\left(\frac{u_{20}^3 C_p}{T}\right). \tag{3}$$

Here σ and C_p are the entropy per unit mass and heat capacity per unit mass at constant pressure, respectively. Near T_λ, $\alpha_2 \sim (C_p t)^{-1}$. To within 3%, $C_p\alpha_2/\sigma T = -0.47 t^{-1}\,\mathrm{K}^{-1}$ over the range $10^{-8} < t < 10^{-2}$. The factor of $\sigma T/C_p$ varies from 0.14 to 0.37 K over the same range of t. The approximate proportionality of α_2 to t^{-1} indicates that the nonlinearities will be apparent even for the smallest amplitudes of v_n if t is small enough. In our fits, α_2 was of course evaluated using the full expression Eq. 3.

Burgers' equation can be shown to result from an expansion to lowest nonlinear order of the equations of Landau two-fluid hydrodynamics.[28–30] It describes only pulses traveling in one direction, and not a pulse that interacts with itself, for example, as it reflects off of a wall (for a further discussion, see Ref. 3).

The data in this experiment is the temperature of the bolometer as a function of time, and the power input at the heater. A model of second sound propagation in bulk helium is therefore not quite sufficient for analyzing the measurements. Careful accounting of thermal effects in the heater and bolometer substrates are also required.

In the analysis, either the pulse that is launched at the heater, or the first pulse detected at the bolometer, may be used as an initial condition for the solution of Burgers' equation. The solutions are fit to the pulse measured at a later time, that is, at a later arrival at the detector (a later echo). Fits done with the heater pulse as an initial condition were quite sensitive to small errors ($< 1\%$) in the bolometer calibration, or to errors in the parameters chosen for the substrate model (i.e., the thermal conductivity or Kapitza resistance of the boundary), and so they were only used to aid in choosing a Kapitza resistance and for doing the dynamic calibration of the bolometers. The fits involving only bolometer data were quite insensitive to the value of the Kapitza resistance chosen, and even to errors as big as 5% in the bolometer calibration. The only two adjustable parameters in these fits were u_{20} and D_2. Since these were the only parameters involved and since there was little correlation between them, they could be determined with considerable precision, and deviations from Burgers-like behavior was easily spotted.

The best value for the Kapitza resistance of the bolometer and heater substrates was 0.5 $\mathrm{cm}^2\mathrm{K/W}$. The parameters for the Pyrex substrates[32,33] are those of Ref. 3; the heat capacity and thermal conductivity were 0.03 J/kg K and 0.05 W/mK, and the density was 2230 $\mathrm{kg/m}^3$.

Fits were performed using a wide variety of initial and final conditions; the same data set could of course be fit using any early pulse as an initial condition and any later pulse as a final condition. There were limits to this procedure for pulse sequences taken at very small t, where temperature fluctuations of a few nK lead to small but evident fluctuations in the arrival times of the later echoes. This leads to a "smearing" of these echoes in the averaged pulse sequence, which manifests itself as a slightly larger damping and velocity. However, outside of this small-t regime there were no noticeable effects due to choice of fitting pulse, and the choice is somewhat arbitrary. For the data compiled in Appendix A and discussed throughout this section, the first arrival of the pulse at the bolometer was always used as an initial condition for the model. For data at $t < 9 \times 10^{-6}$, the second echo was used in the fit. For $9 \times 10^{-6} < t < 9 \times 10^{-5}$, the third echo was used in the fit, and for all other data, fits were done to the fourth echo.

Since later pulses have self-interacted (at reflection off the cell walls) more times than earlier ones, the absence of a trend of the fitting parameters with echo number can be taken as evidence of the unimportance of interaction effects. A further discussion and search for interaction effects is discussed below.

Throughout this work, the validity of the model near T_λ is investigated. In the next section we discuss some necessary conditions for the applicability of Burgers' equation as well as the effect of interactions. In Sec. IV, results are presented, and in Appendix A the values obtained for u_{20} and D_2 are tabulated. These data were taken under a great variety of conditions, and except in the most extreme cases (very large or very long pulses, for example), the fitting parameters (u_{20} and D_2) were independent of these conditions. This is a good indication, but of course not a proof, that the model used in the analysis is valid and that relevant nonlinear terms are properly taken into account.

3.2. On the Use of Burgers' Equation Near T_λ

The truncation of the expansion which leads to Burgers' equation is expected to hold only if $\delta\rho_s/\rho_s \ll 1$. Upon approaching the λ-point, we have $\rho_s \sim t^\zeta$. Thus the condition for Burgers' equation to still be applicable to our second-sound pulses can be written $\zeta \delta t/t \ll 1$ where $\delta t/t$ is the temperature amplitude of the pulse expressed as a fraction of t. While this is a necessary condition, it is not sufficient. A variety of other effects come into play, and some may be enhanced near the transition.

A problem which potentially becomes more severe near T_λ is linear coupling to first sound. We have no method for detecting first sound in this experiment. However, there are two dimensionless parameters that

characterize this coupling,[34,35] $(1-C_v/C_p)$ and the ratio (c_2^2/c_1^2), where c_1 and c_2 are the perfectly decoupled $(1-C_v/C_p=0)$ values of the first and second-sound velocities

$$c_1^2=\left(\frac{\partial P}{\partial \rho}\right)_\sigma \tag{4}$$

and

$$c_2^2=\sigma^2\frac{\rho_s T}{\rho_n C_v}. \tag{5}$$

Here P is the pressure, ρ the density, C_v the heat capacity at constant volume, and σ the entropy per unit mass. The parameter $1-C_v/C_p$ is always quite small for ^{4}He at vapor pressure, but its value increases near T_λ. An estimate[36] gives $1-C_v/C_p\approx 0.05$ at $t=10^{-7}$ and SVP. The expression for the linear second-sound velocity that we use in Eq. (2) already contains the term linear in $(1-C_v/C_p)$. The next term is of order $(1-C_v/C_p)(c_2^2/c_1^2)$. The ratio $c_2^2/c_1^2=1.3\times 10^{-3}$ at $t=10^{-2}$, and it falls as we approach T_λ and c_2^2 goes to zero. The second term is therefore always quite small and can be ignored, even very near T_λ. Higher order terms all contain powers of c_2^2/c_1^2, and are therefore smaller yet.

In an effort to minimize some of the nonlinear effects, we will limit our use of the model to second-sound pulses whose temperature excursions are less than 10% of the distance to T_λ; that is, the amplitude of the pulse used as an initial condition, δt, is related to t by

$$\delta t<0.1t. \tag{6}$$

Even with the limit imposed by Eq. (6), there are nonlinear effects not included in Burgers' equation. As discussed in Ref. 3, the nonlinear coupling to first sound[37] is ignored. This coupling appears to remain quite small near T_λ, but a further experimental or theoretical investigation is in order.

Of greater concern is the influence of the nonlinear interaction of the pulse reflecting through itself. Burgers' equation does not account for these effects, but testing for their presence is straightforward. One method, used successfully farther from T_λ in Ref. 3, is demonstrated in Fig. 4. In this technique, two pulses are launched in rapid succession from the heater. At the first arrival of the double pulse at the bolometer, the first pulse has interacted only with itself (as it reflects off the boundary) while the second pulse has interacted with the reflected first pulse as well as with itself. The two pulses many be directly compared, and any disparities in their shapes

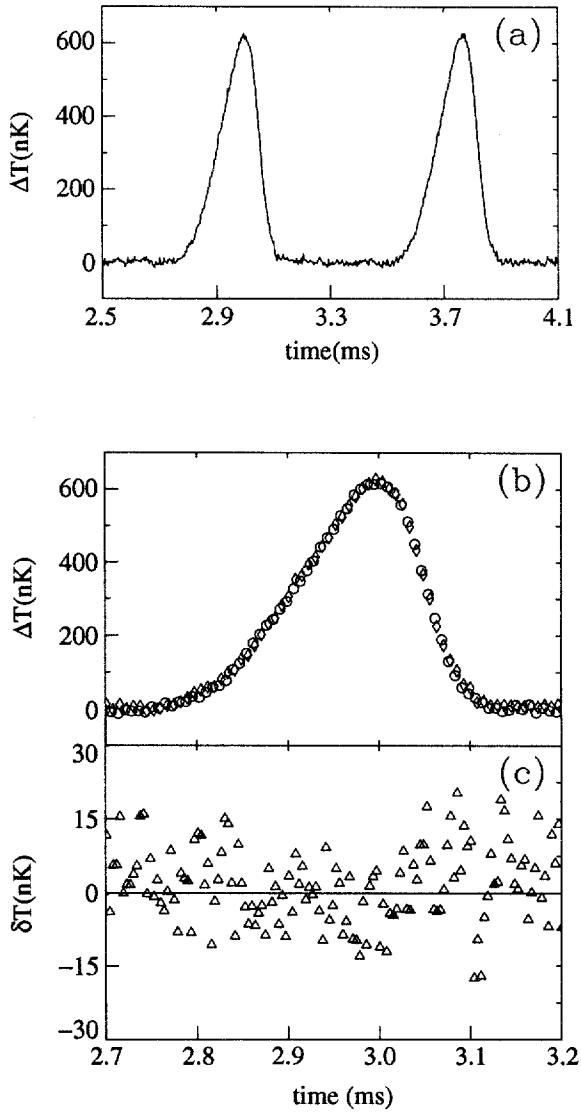

Fig. 4. The absence of distortion due to pulse interactions is demonstrated. For these data, $t = 4.9 \times 10^{-6}$ and the initial pulse length is 0.12 mm. The first arrival of a double pulse at the bolometer is shown in (a). The open diamonds in (b) are the first pulse in (a) replotted, and the open circles are the second pulse, shifted in time to coincide with the first pulse. The difference between these two pulse shapes are shown in (c).

or arrival times is taken as evidence of an interaction effect. For the data in Fig. 4, the reduced temperature is 4.9×10^{-6} and the *initial* pulse widths[38] are 0.12 mm although they have spread (and are closer to 0.2 mm) upon their first arrival at the detector. The amplitudes of the pulses are near $\delta t/t = 0.03$. Figure 4(a) shows the actual data for the first arrival of the pulse pair. For Fig. 4(b), the second pulse has been shifted along the time axis to coincide with the first using a least-squares algorithm. The resulting pulses and their differences [Fig. 4(c)] are plotted.[39] The agreement between the two pulses is excellent, and the arrival time of the second pulse at the bolometer is unaffected by the existence of the first pulse. We conclude that self-interaction does not play a significant role here. Larger amplitudes ($\delta t/t \approx 0.06$) were also used. Double pulse sequences were done for t as small as 3×10^{-6}, and there were never any significant differences between the first and second pulses for the small-amplitude pulses used to determine sound velocity and damping.

In order to further check for interaction effects, data were generally taken at a variety of pulse widths, and systematic deviations of the measured velocity and damping were sought (examples are given in Figs. 5 and 6). For an infinitesimally short pulse, interaction effects are expected to be minimal. As mentioned above, the absence of any noticeable effect of the fitting parameters on the echo number used in a fit is also evidence against significant interaction effects.

Higher order nonlinear effects should not be important as long as $\delta t/t$ remains small. As we approach T_λ, we will of necessity be working at successively larger values of $\delta t/t$. In order to check for any systematic dependence of second-sound velocity or damping on pulse amplitude, most of the data was taken at two or more amplitudes. Systematic deviations of D_2 were in fact noticeable at sufficiently high amplitudes, but they always showed up first as a small but obvious deviation from a fit to the model. Similarly, a sufficiently long pulse, even at very low amplitude, inevitably seems to deviate slightly from Burgers-like behavior. The fact that this happens even at quite small amplitudes is perhaps evidence of yet another class of effects coming into play near T_λ. The formation of vortices and the effects of superfluid turbulence have been the subject of much interest, but little work has been done in the region very near T_λ. Such effects are ignored in the two-fluid hydrodynamics used to derive Burgers' equation. This topic will be discussed further in Sec. 7; for now it is sufficient to say that any amplitude or pulse-width dependence of the second-sound velocity or damping is easily detected in these experiments, and we find a large regime where such effects are unimportant.

4. RESULTS

Data were taken at a great variety of (initial) pulse amplitudes and (heater) pulse lengths for reduced temperatures between 10^{-2} and 10^{-6}. Inside of 10^{-6}, the small amplitude of the signals required that we signal averaged for as long as 16 hours. The ^{4}He melting pressure thermometer was typically stable to a few nK over hours:[20] nonetheless, the difficulty of data taking increased near T_λ and so for $t < 10^{-6}$ data was typically taken at only a single pulse-amplitude and length. The length and amplitude used were chosen to be consistent with pulses well described by the model for $t > 10^{-6}$, as will be discussed below. The results for u_{20} and D_2 are compiled in Appendix A.

4.1. Results at Different Pulse Lengths

Although the damping of second sound is independent of k (the wavenumber of the sound), the attenuation is dependent on k^2 and so the shorter the pulse, the more sensitive it is to the effects of D_2. This is particularly evident in the region $t > 2 \times 10^{-5}$, where the damping is still quite small and the longer pulses are particularly insensitive to the effects of D_2.

Several examples are shown in Fig. 5. In each case, the open circles are the temperature of the bolometer at the fourth arrival of the pulse (nominally a factor of two larger than the temperature change in the helium, see Section 3). The line is a best fit using the first pulse arrival as an initial condition. The only parameter varied at the heater is pulse length; the heater voltages are nominally the same. The solid circles below each fit are the residuals (the fit values subtracted from the data). The pulse lengths and fit parameters are given in Table 1. For the very longest pulse, (a), the fits are quite insensitive to the value of D_2 and this fit is therefore not used in the compilation of D_2. There are also small but systematic residuals present in this pulse; this "bowing" is typical of these longest pulses and becomes more pronounced closer to the λ-point and at higher amplitudes. The pulse shown in (b) is quite sharp, so much so that there are numerical difficulties involved in the calculation (which are responsible for the spike in the residuals), and the second-sound damping has been artificially raised by the fitting procedure in order that the numerics do not altogether blow up. Closer to T_λ, as the damping grows, this is no longer a problem. Pulse lengths greater than 0.20 mm were never used for $t > 10^{-5}$, but lengths as large as 0.34 mm worked quite well for smaller reduced temperatures. The largest pulse lengths tested, near 0.60 mm, nearly always showed the systematic residuals shown in (a), and were also

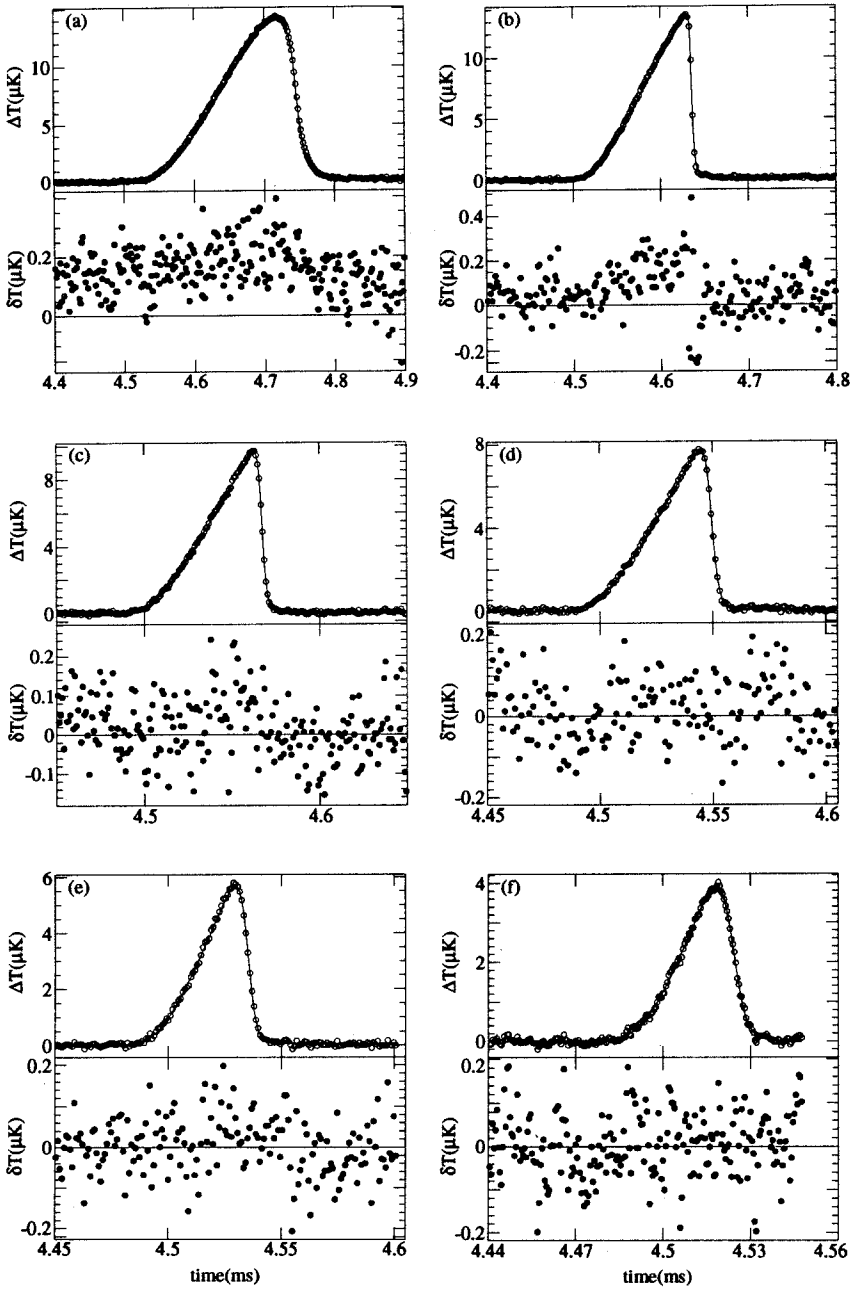

Fig. 5. Examples of second-sound data and fits at $t = 2.54 \times 10^{-4}$. In each case, the open circles are the temperature recorded at the detector for the fourth pulse echo, the line is the best fit using the first arrival of the pulse at the bolometer as an initial condition, and the fit residuals are shown (solid circles) below. A variety of pulse lengths are shown; see the text (and table 1) for a description. Only (c)–(f) were used to find the second-sound velocity and damping.

TABLE I

Fitting Parameters for Fig. 5a to f

$t = 2.541 \times 10^{-4}$				
Fig. 5	pulse length	u_{20} (m/s)	D_2 (10^4 cm^2/s)	δD_2 (10^4 cm^2/s)
a	0.60 mm	1.875	2.54	0.36
b	0.30 mm	1.875	5.13	0.07
c	0.121 mm	1.875	4.56	0.05
d	0.080 mm	1.875	4.59	0.06
e	0.050 mm	1.875	4.57	0.06
f	0.030 mm	1.875	4.38	0.06

plagued by numerical difficulties somewhat closer to T_λ, and so were never used in the determination of u_{20} and D_2. As the pulse length decreases, the pulses form shock tails faster, but the increased attenuation also tends to round the shock.

It is interesting to notice that the sensitivity of D_2 of these fits in fact *depends* on the nonlinear terms; the loss in the integrated power carried by these pulses due to attenuation cannot be measured. For example, for the fit shown in Fig. 5(f) (with the highest frequency components and therefore the greatest attenuation), an integration of the initial pulse (first echo) yields an energy content of 0.166 mJ; an integration of the fourth echo yields 0.168 mJ. The difference is within the error of about 2.5%. Thus the energy carried by the pulse does not decay in a measurable fashion between the first and the fourth echo. Only the change in pulse shape as it evolves in a nonlinear fashion is affected by D_2. In the linear case there is no evolution of the pulse shape for these short times and therefore no sensitivity to the damping.

Finally, we mention that although u_{20} is unaffected by the difficulties described above, we nonetheless do not use the fits shown in (a) and (b) for a measurement of u_{20}, either.

The fits shown in Fig. 5(c)–(f) are all quite good, with no systematic residuals. There is good agreement among the resulting values of D_2, and excellent agreement among the resulting u_{20}'s.

The smallness of D_2 prevents its measurement by this method for $t \geqslant 5 \times 10^{-4}$. For small damping, the pulses are either completely insensitive to the value of D_2 (for small amplitudes and the longest pulses), or numerical difficulties illustrated in Fig. 5(b) persist to the shortest available pulse lengths. While good values for u_{20} are attainable even in the linear regime by this method, values for D_2 are not. We are limited in how short a pulse we can use by the bandwidth of the electronics; higher frequency

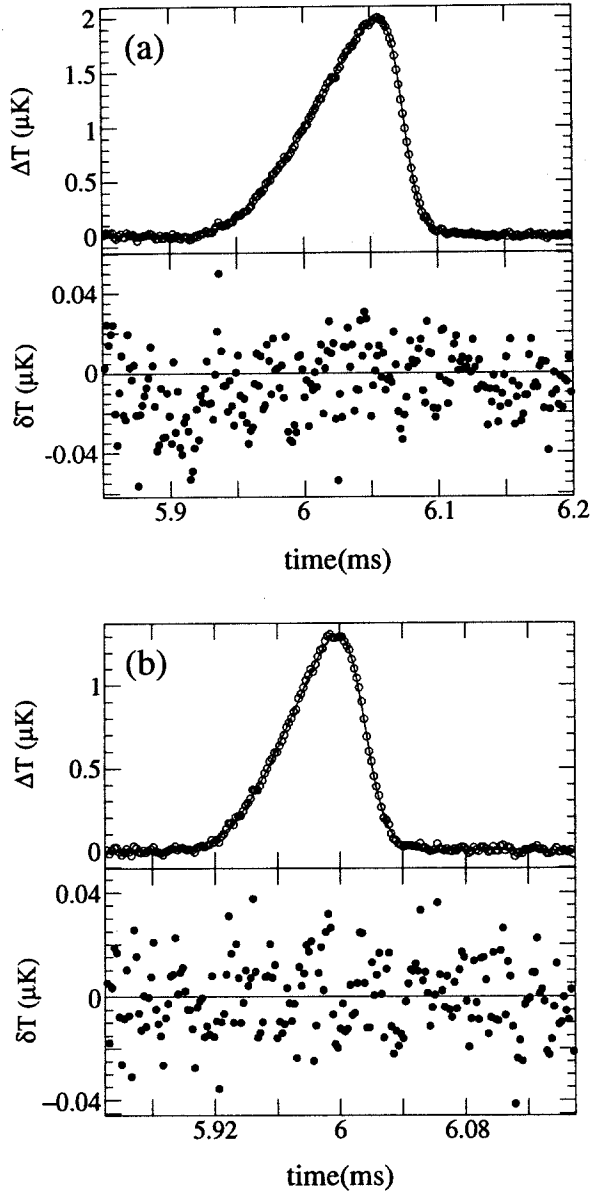

Fig. 6. Typical fits, used to determine u_{20} and D_2 at $t = 5.015 \times 10^{-5}$. The initial pulse length was 0.160 mm (corresponding to a 6336 Hz haversine) for the pulse shown in (a) and 0.080 mm (12672 Hz) for the pulse shown in (b). In both cases, the open circles are the temperature recorded at the detector for the third pulse echo, the line is the fit using the first arrival of the pulse at the bolometer as an initial condition, and the fit residuals are shown (solid circles) below. For both fits, $u_{20} = 1.015$ m/s.

response would presumably allow us to measure D_2 even in this regime. Here, the shortest useable pulse length, shown in Fig. 5(f), corresponds to a single cycle of a 62,210 Hz haversine. Note that the bandwidth must be such that quite high harmonics of this frequency remain unattenuated if electronic pulse distortion is to be avoided.

Some typical data used to determine u_{20} and D_2 is shown in Fig. 6. Here $t = 5.015 \times 10^{-5}$ and initial pulse lengths of 0.160 mm (a) and 0.080 mm (b) are shown. The initial pulse amplitudes are again nominally the same.

4.2. Results at Different Pulse Amplitudes

Data were also taken at a variety of initial pulse amplitudes. An example is shown in Fig. 7 for $t = 6.34 \times 10^{-6}$. Here the widths of the pulses launched at the heater are the same for each different amplitude shown, and only the amplitudes have been varied. In all the data, the larger-amplitude pulses develop sharper trailing edges and spread more. This is as expected, since the larger the sound amplitude, the smaller the local sound velocity.

The pulses shown in Fig. 7 were typical of those used in the fits for u_{20} and D_2. Pulses with relative amplitudes $\delta t/t$ that were near (but still less than) 0.1 began to display the same apparent "bowing" evident for the longest pulses in Fig. 5. More severe examples, at even larger amplitudes, are discussed in Sec. 7. The pulses used in the study of u_{20} and D_2 ranged in amplitude from $\delta t/t = 8.1 \times 10^{-4}$ to $\delta t/t = 0.066$. As we moved away from T_λ, it was necessary to use smaller and smaller relative amplitudes; the small damping at large t meant that large pulses got very sharp very fast and were numerically difficult to model.

We are ultimately limited in how close to T_λ we can work by the sensitivity of our detector. Near $t = 3 \times 10^{-7}$, we can still measure weakly nonlinear pulses with 12 hours or more of signal averaging. The data point at smallest t is shown in Fig. 8. Here $\delta t/t = 0.057$. The noise is relatively large, but the pulse shape is quite sensitive to the large damping and for the velocity measurement the noise is immaterial. Larger pulses might have a better signal-to-noise ratio, but would fall outside the validity of our model.

Since only single data sets were taken at each reduced temperature less than 10^{-6}, some effort went into choosing reasonable pulse widths and amplitudes. Values of $\delta t/t$ were generally no bigger than those which had already worked well in the 10^{-6} decade. Pulse widths could not be too short; the damping here is quite large and shorter pulses (with their higher frequency components and therefore larger attenuation) get quite small very fast. In order to be able to see a signal at all, we found that initial

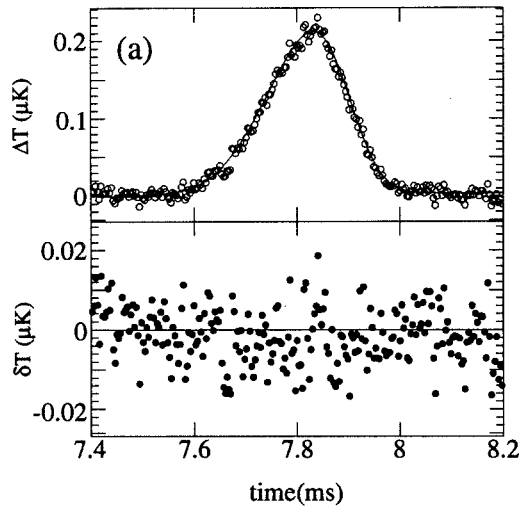

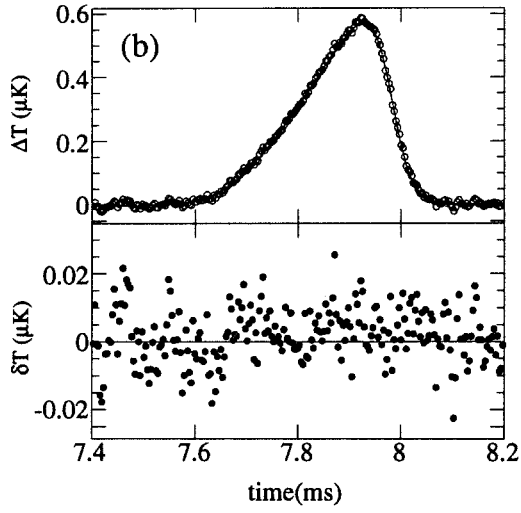

Fig. 7. Examples of second sound fits near $t = 6.34 \times 10^{-6}$. The maximum amplitude of the initial condition was $\delta t/t = 0.012$ for the fit shown in (a), and 0.031 for (b). The initial pulse lengths were 0.12 mm. The fits resulted in $u_{20} = 0.4721$ m/s, $D_2 = (14.3 \pm 0.2) \times 10^{-4}$ cm^2/s at $t = 6.348 \times 10^{-6}$ for (a), $u_{20} = 0.4719$ m/s, $D_2 = (12.8 \pm 0.2) \times 10^{-4}$ cm^2/s at $t = 6.335 \times 10^{-6}$ for (b).

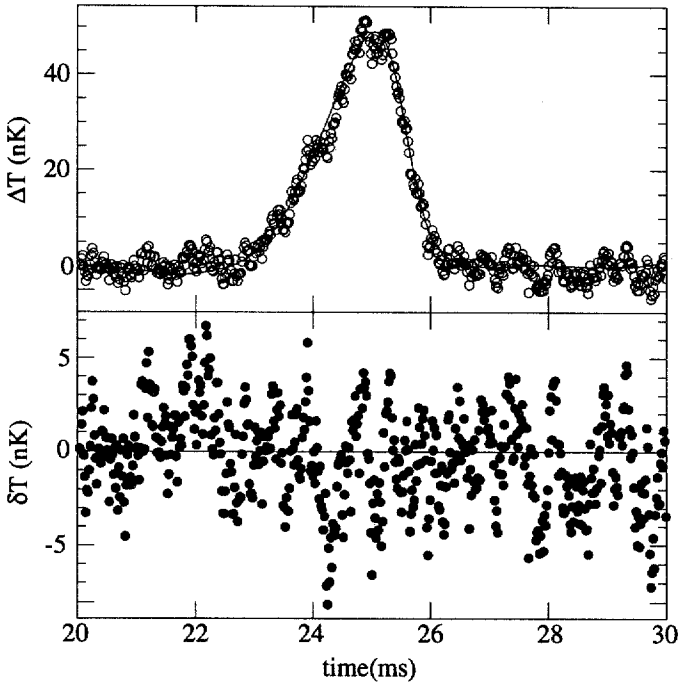

Fig. 8. Second arrival of the pulse at the bolometer and fit for $t = 3.07 \times 10^{-7}$. Here the pulse width at the heater was 0.32 mm and the amplitude of the first echo, used as an initial condition, was $\delta t/t = 0.057$. This fit gave $u_{20} = 0.1553$ m/s. A pulse was launched at the heater every 1.3 s and pulse sequences at the bolometer were averaged for about 10 hours in order to achieve the 3 nK resolution shown.

pulse lengths had to be kept near the maximum value shown to work for $t > 10^{-6}$, that is, near 0.30 mm.

A complete compilation of the data satisfying all the requirements discussed above is found in Appendix A. The values for u_{20} were "normalized" to the data of Greywall and Ahlers[1] at $t = 10^{-2}$; i.e., the cell length was determined, using the previously measured value of u_{20} at a reduced temperature of 10^{-2}, to be 0.1203 ± 0.0001 cm.

4.3. The Effect of the DC Heat Flux at the Bolometer

The detector used in this experiment is a dissipative device, its sensitivity increasing with increased power dissipation.[3] The velocity of second sound is predicted to decrease in the presence of a counterflow,[40,41] until it reaches zero at a "critical" heat flux, Q_c. In order to directly check for any

effect of the heat flux at the detector on the second sound, data were taken at 0.52 and 0.043 μW (8.0 and 0.67 μW/cm^2, see Ref. 42), a factor of 12 apart, in the region $1\times10^{-6}<t<5\times10^{-5}$. No significant differences in pulse shape, velocity, or damping were found in the region $3\times10^{-6}<t<5\times10^{-5}$. It was not necessary to check for systematic deviations farther from the λ-point, since Q_c is known to increase with increasing t. Nonetheless, occasional runs were done at various bolometer powers and no systematic effects were noted for $t>5\times10^{-5}$, either.

For $t\leqslant3\times10^{-6}$, and for the larger bolometer power, the pulses began to develop large tails. An example of a pulse sequences near $t=1.6\times10^{-6}$, at two different bolometer powers, is shown in Fig. 9. Figure 9(a) is taken at a power of 0.52 μW, while 9(b) shows a pulse sequence taken with a bolometer power of 0.043 μW. For $t>3\times10^{-6}$, the tail disappears and the two dissipations give identical signals. For $t\leqslant3\times10^{-6}$, only the smallest bolometer power, 0.043 μW, was used, and no tails were ever observed on the pulses used to measure u_{20} and D_2 (See, however, Sec. 7 for a discussion of larger-amplitude pulses).

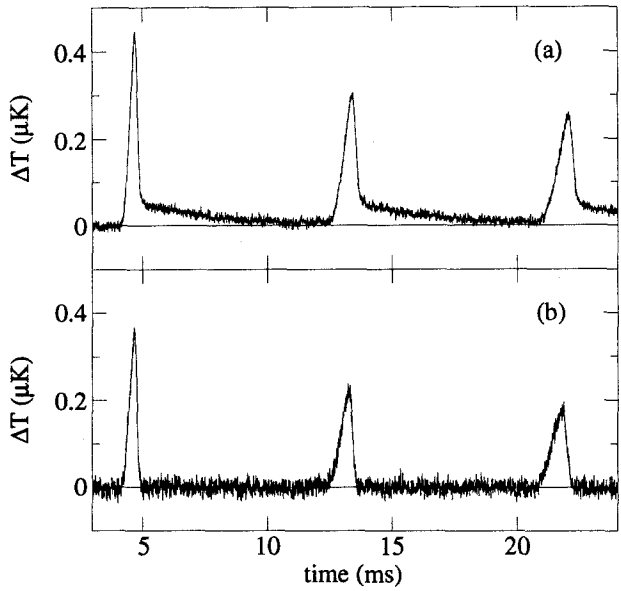

Fig. 9. The effect of increasing the DC heat flux at the bolometer is shown. Here $t=1.6\times10^{-6}$ and the voltage pulse across the heater is nominally the same in (a) and (b). For (a), the bolometer power was 0.52 μW, for (b), 0.043 μW.

4.4. The Effect of a DC Heat Flux at the Heater

For all pulses used in the analysis of second-sound velocity and damping, the dc heat flux Q at the heater was zero. A short study was also done varying Q. With increasing Q, u_{20} is expected to decrease and go to zero for $Q = Q_c$.[40,41]

There was no evidence of a systematic shift of u_{20} with bolometer power, although there was a significant effect when a similar dc heat flux was applied at the heater. This can be attributed to the geometry of the cell. The bolometer is quite a small device (see Sec. 2), about 0.25 cm on a side. The cell is quite broad and flat, and the bolometer looks out onto an area of 10 cm^2. Any heat flux from the bolometer is quickly dispersed in the cell volume. In contrast, the heater covers the same area as an end of the cell (10 cm^2) and a heat flux emanating from the heater cannot disperse. On the other hand, a dc heat flux at the heater can hardly be expected to create a uniform dc flow in the cell, since it must leave the cell around the mylar spacers at the edge of the bolometer and heater substrates (Fig. 2). Nonetheless we do measure an effect that is of the expected form, if not of the expected size.

The results of this study are shown in Fig. 10 as solid cricles. For $t = 6.31 \times 10^{-6}$, a series of pulse sequences was taken at various dc heater powers. All other variables, such as pulse amplitude ($\delta t/t \approx 0.03$) and the frequency of the haversine used to generate the pulse, were held constant. As expected, the second-sound velocity drops with increasing heat flux. For $Q = 3.06\ \mu W/cm^2$, no second sound was detectable.

Near T_λ the velocity of second sound in a counterflow can be written[40,41]

$$u_2 = -aw + \left(1 - \frac{w^2}{w_c^2} + \frac{(aw)^2}{u_{20}^2}\right)^{1/2} u_{20}. \tag{7}$$

Here the counterflow velocity w in the direction of second-sound propagation and the heat flux Q are related by the usual expression (for zero mass current)

$$Q = \rho_s(w)\, STw \tag{8}$$

except that the superfluid density, $\rho_s(w)$, is also a function of the counterflow velocity w. In order to complete the relationship between counterflow and heat flux, we need an expression for $\rho_s(w)$. For temperatures close to T_λ, we can use[43–46]

$$\rho_s(t, w) = \rho_s(t)\left(1 - \frac{w^2}{3w_c^2}\right) \tag{9}$$

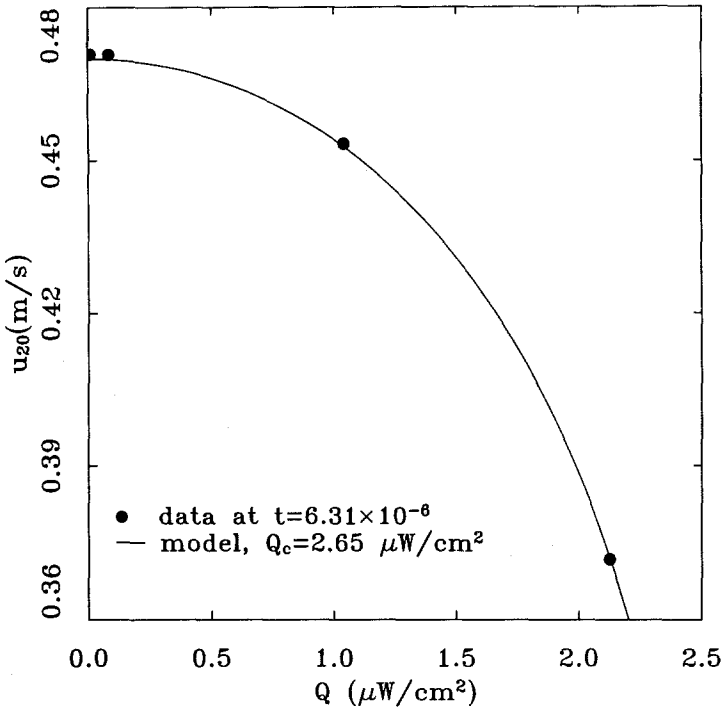

Fig. 10. The effect of a DC heat flux at the heater on the velocity of second sound. The solid circles are the data. The solid line is the result from Eq. 7 with a critical heat flux, $Q_c = 2.65\ \mu\text{W/cm}^2$.

where $\rho_s(t)$ is just the usual superfluid density (in zero counterflow) discussed in Sec. 6. Finally, our value for a is determined from thermodynamic parameters as discussed in Ref. 40.

The line in Fig. 10 is the velocity of second sound predicted[47] by Eq. (7) with a critical heat current $Q_c = 2.65\ \mu\text{W/cm}^2$. This value of Q_c is about two orders of magnitude smaller than expected from the predictions of Refs. 40 and 41, although the qualitative behavior of u_{20} agrees with the theory.

While the geometry of the cell prevents us from drawing any quantitative conclusions about Q_c from this study, it is perhaps surprising that the discrepancy between theory and experiment is so large. Further experimental studies are in order. It is apparent that a study of Q_c in this range of t might be carried out with little difficulty in a modified geometry, i.e., one that allows through flow of the dc heat flux. With such data, an analysis that exploits the renormalization group analysis of Ref. 41 is clearly in order.

4.5. The Effect of Gravity

In the presence of gravity, the hydrostatic pressure of a column of helium causes a shift in T_λ of about 1.273 μK/cm.[25] This means that the reduced temperature in a sample cell is a function of the vertical position, and therefore the second-sound velocity and damping will also vary across the cell. In order to minimize any corrections that need be made due to gravity, and for consistency in defining a reduced temperature both above and below the λ-point, the reduced temperature is always defined relative to T_λ at the cell middle. Furthermore, the sample cell has been mounted in such a way that the planar pulses travel vertically through the cell (see Fig. 2); this is necessary to ensure that the pulses remain planar very near T_λ, i.e., that all points on the wavefront always move at the same local velocity. In addition, the cell used in this experiment was only 1.2 mm tall in order to minimize the effects of gravity. The gravity corrections for this cell are in fact minimal. At $t = 3 \times 10^{-7}$, the smallest reduced temperature for which data is available, the effect on u_{20} was only 0.2%. This is within the error bars of the measurement, so that the effect of gravity can be altogether ignored in this experiment. The calculation of this gravity correction is discussed extensively in Ref. 48.

5. SECOND SOUND DAMPING

5.1. Discussion of Second-Sound Damping Results

The values for D_2 resulting from the fits discussed in Sec. 4 are plotted in Fig. 11, and are tabulated in Appendix A. The errors are the 67% confidence limits. Values were obtained for $3 \times 10^{-7} < t < 5.1 \times 10^{-4}$. As discussed earlier, data were taken at a variety of second-sound pulse amplitudes and widths, and two different bolometer power levels (0.043 μW and 0.52 μW). It is immediately clear from Fig. 11 that, over the range where both levels were used ($3 \times 10^{-6} < t < 5 \times 10^{-5}$), there is no systematic dependence of D_2 on the bolometer power.

The dependence on pulse width is investigated in Fig. 12. Here the second-sound damping is plotted on the ordinate and the abscissa shows the length of the pulse as it leaves the heater (given by u_{20}/ν). The voltage applied at the heater is the same for each pulse at a given temperature; only the frequency (ν) of the haversine is changed. The data and fits corresponding to the points at $t = 5.01 \times 10^{-5}$ can be found in Fig. 6. For the data at $t = 2.54 \times 10^{-4}$, the corresponding second-sound fits and data are shown in Fig. 5, and the results are given in Table 1. There are clear discrepancies visible for pulse widths near 0.30 mm and 0.60 mm at $t = 2.54 \times 10^{-4}$. As

noted above, pulses with lengths greater than 0.20 mm were never used at reduced temperatures greater than 10^{-5}, and pulse lengths greater than 0.34 mm were never used at all in the compilation of the data shown in Fig. 11 and Appendix A. No systematic trends with pulse width were found over the range of data used in the measurement of D_2.

The dependence of D_2 on pulse amplitude is investigated in Fig. 13. D_2 is again plotted on the ordinate while $\delta t/t$, the amplitude (expressed as a fraction of the distance to T_λ) of the pulse used as an initial condition in the model, is plotted along the abscissa. Here the pulse lengths at the heater are the same for the points shown at each temperature, except for the data at $t = 3.98 \times 10^{-4}$, for which two pulse lengths (different by less than 20%) were used. A corresponding fit and parameters for the data at $t = 6.35 \times 10^{-6}$ shown in this figure are given in Fig. 7.

For most of the data shown in Fig. 13, the fits at various amplitudes

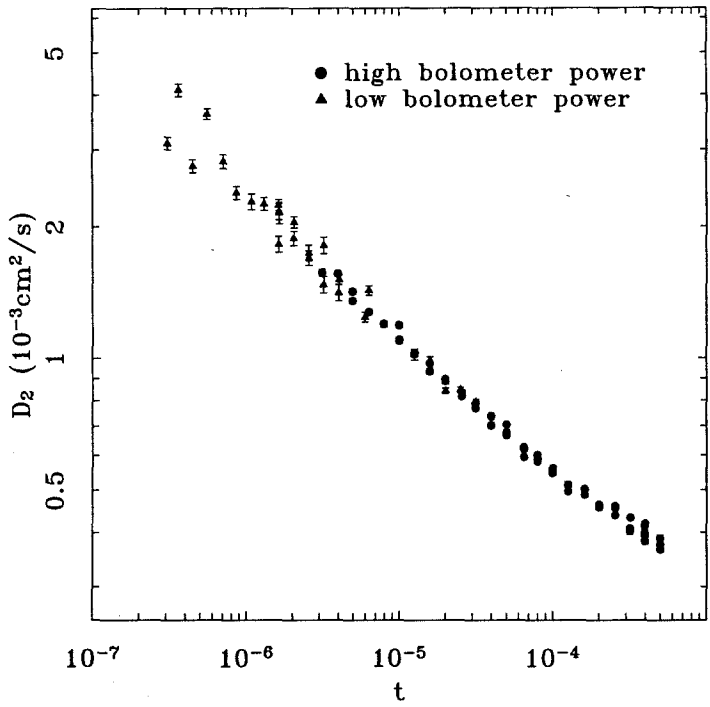

Fig. 11. The second-sound damping, D_2. The solid circles are data extracted from second-sound data taken with a power at the bolometer of 0.52 μW. The solid triangles are from data taken with the bolometer dissipating 0.043 μW.

give values for D_2 that are self-consistent; that is, the values do not vary by more than about twice the error bars. There are three exceptions. The first, at $t = 3.98 \times 10^{-4}$, probably has to do with the relative insensitivity of the fits to D_2 in the region where D_2 is small, and the error bars given by the fit may well be underestimated. The slight inconsistency between the points measured at $t = 3.19 \times 10^{-4}$ may also have to do with the small value of D_2 in this region. As discussed earlier, just slightly farther from T_λ, above $t = 5.1 \times 10^{-4}$, this methods becomes quite useless for measuring D_2. Certainly there is no overall trend with increasing amplitude; the scatter at these temperatures in Fig. 13 appears random. Another discrepancy exists at $t = 10^{-5}$. Here the amplitude of the pulse, $\delta t/t$ is very nearly 0.1 and the data showed significant deviation from Burgers-like behavior. Points at such large amplitudes were not used in the compilation of the D_2 data.

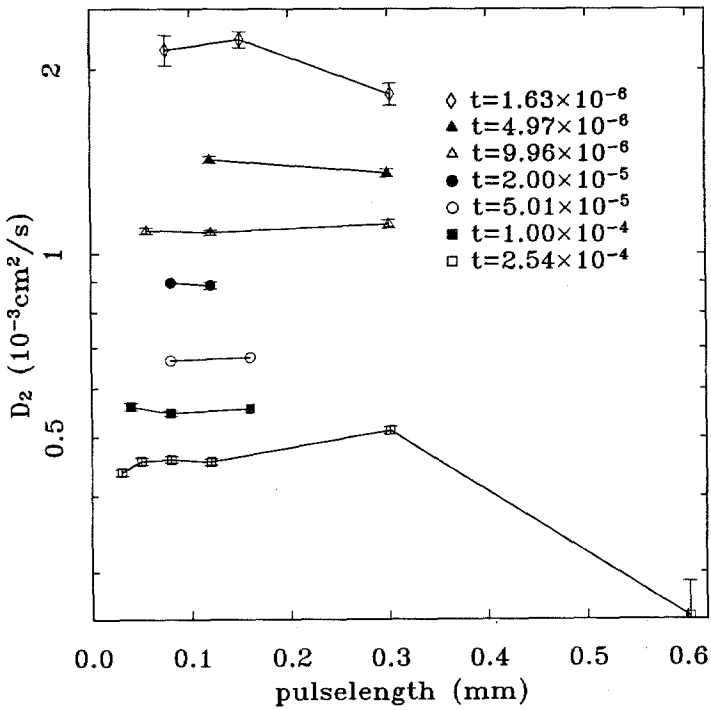

Fig. 12. Demonstration of the dependence (or lack thereof) of D_2 on pulse width. Data taken at a variety of temperatures are shown. For each temperature, the heater voltage is held constant. Only the pulse widths are changed.

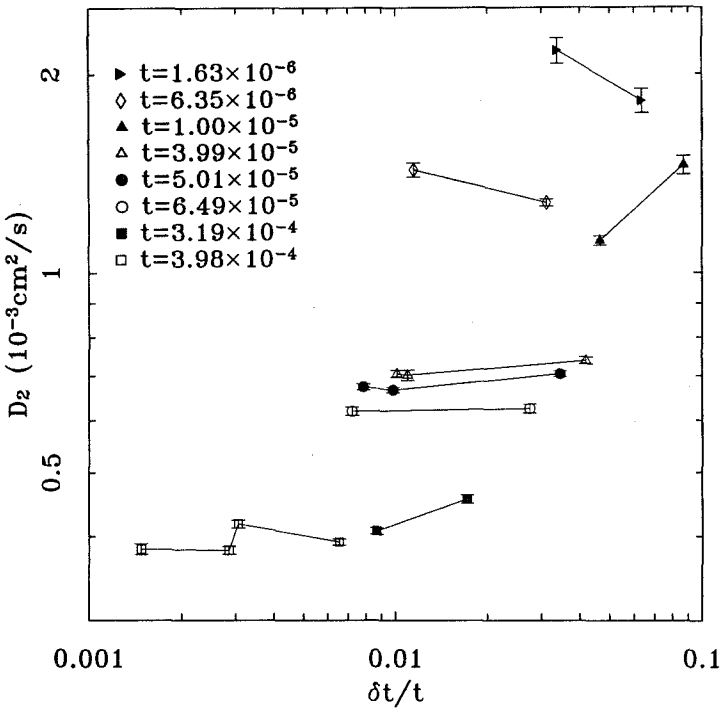

Fig. 13. Demonstration of the dependence (or lack thereof) of D_2 on pulse amplitude. Here $\delta t/t$ is the amplitude of the first pulse echo expressed as a fraction of the distance to T_λ.

5.2. Comparison with Previous Data

The data set shown in Fig. 11 extends, by nearly two decades in t, previous measurements of D_2 at saturated vapor pressure.[49–51] A comparison of these earlier results with each other can be found in Ref. 51. For $t < 10^{-2}$, the agreement among them is quite good, and for $t < 10^{-3}$, the agreement is "much better than could have been expected on the grounds of the error estimates."[51] A comparison is shown in Fig. 14 with one of these data sets.[51] The points taken at 0.3 bar are expected to be systematically lower than the result at SVP by about 1%. Within the larger error bars of previous measurements,[49,50] this suppression was not noticeable. Here a suppression is clearly visible, and is somewhat larger than 1% for at least three data points. The reason for this small discrepancy is not known at this time.

It is interesting to note that the data in each case was taken by a different technique, requiring different methods of analysis. In Ref. 49, a

resonance technique was used and line widths were measured. The analysis included corrections for thermal losses at the sidewalls and losses at the porous detector. Crooks and Robinson[50] also used a resonance technique, but measured the decay time of their cavity instead of line widths. Their corrections included thermal losses at both cell sidewalls and ends. In Ref. 51 the amplitude decay of a "tone burst" of second sound was employed to determine the damping. That technique was not unlike the one used in this experiment, except that the "pulses" consisted of many cycles of a sine wave, and the analysis was done in the linear regime and involved only a measurement of the echo amplitudes. It required the same corrections used by Crooks and Robinson, as well as a correction for diffraction losses. For the current data, the geometry of our experiment is such that the sidewalls do not ever play a role and any losses at the endwalls are implicit in the model. Diffraction losses are negligible in this experiment.[3] In view of these diverse experimental methods, the good agreement in the temperature range of overlap between the different experiments is gratifying.

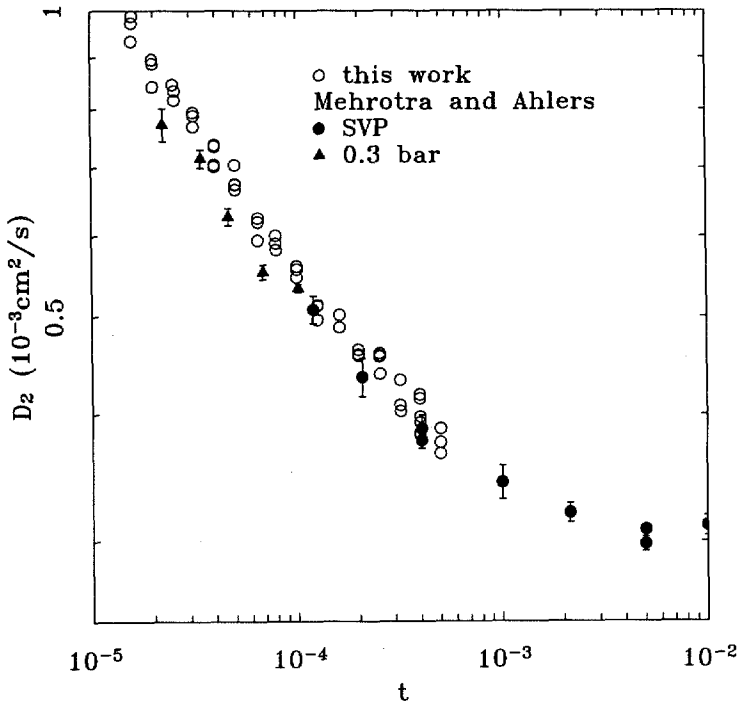

Fig. 14. A comparison of the data set presented here with the work of Mehrotra and Ahlers.[51] The solid triangles are taken at 0.3 bar and D_2 is expected to be slightly lower than at SVP.

5.3. Comparison with Theory

In principle, values for D_2 can be calculated with no adjustable parameters from the results of renormalization group (RG) theory and measurements of the thermal conductivity made only for $T > T_\lambda$. In reality, the full calculation proves quite difficult.

The dynamics of ^{4}He near T_λ are described by Model F of Halperin, Hohenberg, and Siggia.[52] This model contains the four coupling parameters f, w, γ, and u (w is complex, and not to be confused with the counterflow velocity w of Sect. 4.4), two static (γ and u) and two dynamic (f and w), in terms of which the thermo/hydrodynamic properties can be expressed.[53,54] The temperature dependence of the "renormalized" couplings can be calculated from this model given some initial or "background" values away from T_λ. In practice, the background values are evaluated from thermal conductivity data[18] above T_λ.

Recently, the RG recursion relations for the dynamic parameters f and w have been derived by Dohm to two-loop order for model F.[55,56] The recursion relations for the static parameters γ and u were previously derived by Schloms and Dohm.[57] The static relations have been used, along with measured values of C_p for reduced temperatures above T_λ and in the limited region $10^{-4} < t < 10^{-3.5}$, to determine the background values of u and γ.[55] These background values, determined at $t = 10^{-3}$, are then used to evaluate $u(t)$ and $\gamma(t)$ for $10^{-9} < t < 10^{-3}$. Likewise, the background values of f and w are evaluate by Dohm[55] using the thermal conductivity data ($T > T_\lambda$) of Tam and Ahlers[58] (cell F). He then uses these background values and the appropriate recursion relations to determine $f(t)$ and $w(t)$ ($w = w' + iw''$) over the same range. All parameters are tabulated as a supplement to the recent work of Dohm.[55] The recursion relations for w and f involve the parameters u and γ, and so these calculations represent an improvement over previous calculations[58,59] due to the more accurate values for the static parameters.

Once the flow parameters have been evaluated, it still remains to find an expression for D_2. Previous comparisons[51,58] of experimental and theoretical values for D_2 used an expression[60,61] that was calculated within the framework of model E; the *symmetric* planar spin model. In this model, $\gamma = 0$ and the coupling of the order parameter and the entropy in ^{4}He is improperly treated. A recent analysis by Dohm and Schloms[62] and also by Dohm[63] has resulted in an improved form for D_2 that is calculated within the framework of model F. The calculation is a one-loop perturbation expansion, with the leading order terms calculated in model F and the first order perturbation term (one-loop term) calculated within model E. The calculations are performed three different ways, with no way of knowing,

a priori, which is best. Two of the calculations are done in $d=3$ and the last is an expansion in $\varepsilon=4-d$. Dohm and Schloms' formulas[62,63] are summarized below in Eqs. (10)–(16).

The form of D_2 is

$$D_2 = D_\chi + D_\zeta \tag{10}$$

where

$$D_\chi = g_0 \left(\frac{k_B \xi_-}{C_p^-}\right)^{1/2} R_\chi[w(l_-), F(l_-), \gamma(l_-), u(l_-)] \tag{11}$$

and

$$D_\zeta = g_0 \left(\frac{k_B \xi_-}{C_p^-}\right)^{1/2} R_\zeta[w(l_-), F(l_-), \gamma(l_-), u(l_-)]. \tag{12}$$

Here the parameters u, γ, w, and $F=\sqrt{fw'}$ are calculated above T_λ, but evaluated at $l_- = 2t$ where t is the reduced temperature (positive) *below* T_λ, ξ_-, the correlation length[64] above T_λ, is also evaluated at $2t$. C_p^- is the heat capacity per unit volume measured *below* T_λ and evaluated at t. k_B is Boltzman's constant and g_0 is the bare dynamic coupling (given in Ref. 18 to be 2.164×10^{11} s^{-1} at SVP). The dimensionless R_χ and R_ζ have the form

$$R_\chi = R_\chi^0(w, F, \gamma, u)[\Psi_\chi(w', f, u)] \tag{13}$$

and

$$R_\zeta = R_\zeta^0(w, F, \gamma, u)[\Psi_\zeta(w', f, u)] \tag{14}$$

where the leading amplitudes

$$R_\chi^0(w, F, \gamma, u) = (4\pi)^{-1/2} F^{-1}\{1 + \gamma^2[(2u)^{-1} - 4]\}^{-1/2} \tag{15}$$

and

$$R_\zeta^0(w, F, \gamma, u) = w'(4\pi)^{-1/2} F^{-1}\{1 + \gamma^2[(2u)^{-1} - 4]\}^{1/2} \tag{16}$$

are calculated using model F.

The perturbation terms represented by the functions $\Psi_\chi(w', f, u)$ and $\Psi_\zeta(w', f, u)$ have been calculated to one loop order using two different model E formalisms.[62] One is performed in $d=3$ dimensions, and the second is an expansion in $\varepsilon=4-d$. Again, there is no way of knowing, a priori, which calculations will work the best. The various forms of the perturbation terms will be given in Ref. 62 and can also be found in Ref. 17.

The two perturbation expansion results and the zeroth-order term by itself are plotted in Fig. 15 along with our data and that of Ref. 51. The dotted line shows the zeroth-order calculation, where the functions $\Psi_\chi(w', f, u)$ and $\Psi_\zeta(w', f, u)$ have been set equal to one. The "d = 3" and ε-expansion versions of the theory are also shown. There are no adjustable parameters.

Figure 16 shows the same data with the theory calculated using slightly different values for the flow parameters. Here, the γ used is γ^{expt}, which is calculated directly from the values of u and the experimental C_p *below* T_λ (see Ref. 65 for the form of γ^{expt}). The slightly different values for γ give slightly different values for the dynamical parameters f and w. More importantly, the use of γ^{expt} allows the calculation of the flow parameters, and therefore D_2, another decade farther from T_λ.

Figures 15 and 16 show that the best agreement between data and theory is actually for the zeroth order calculation. However, the calculated values of D_2 are not as important as their dependence on t, and for this the

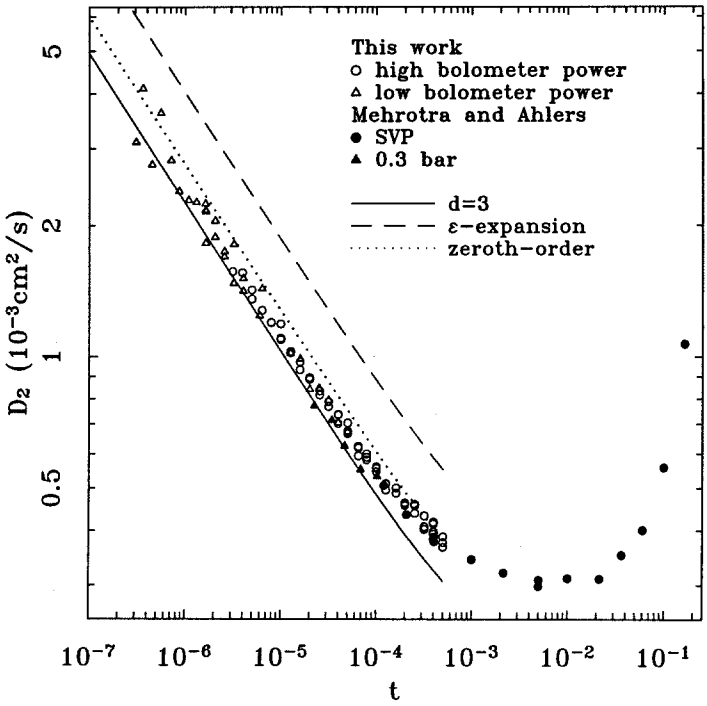

Fig. 15. Results of recent RG calculations for D_2. Three cases are shown (described in text) along with the same data as shown in Figs. 11 and 14. There are no adjustable parameters.

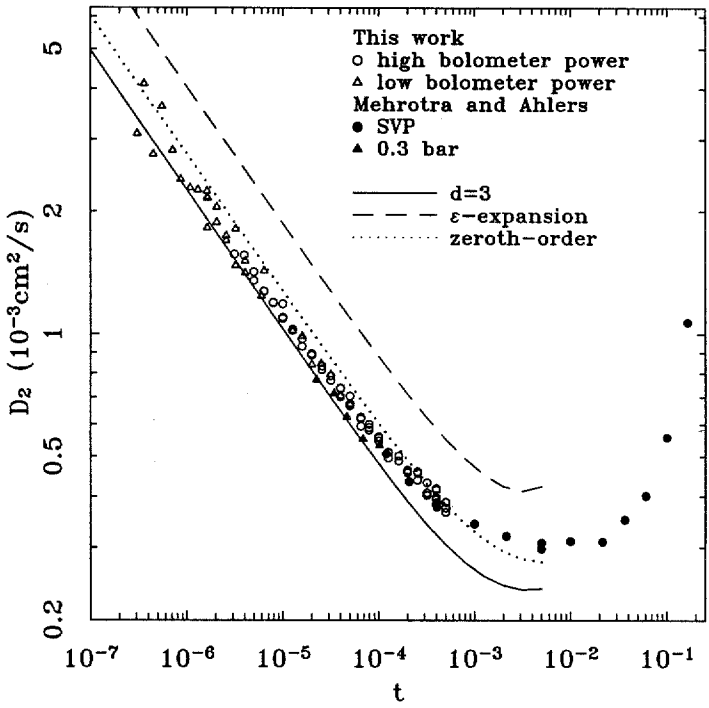

Fig. 16. Results of recent RG calculations for D_2. Here the dynamic flow parameters are calculated using γ^{expt} out to $t = 10^{-2}$. For $t < 5 \times 10^{-4}$, the results are virtually identical to those shown in Fig. 15.

zeroth order and expanded versions are quite similar. Still, there is obvious disagreement between theory and data. Possible candidates for error include the use of model E in the calculation of the perturbation terms; the cutoff of the expression for D_2 beyond one-loop order; the cutoff of the calculation of f and w at two-loop order; or the lack of coupling to first sound in the framework of model F.

6. THE SUPERFLUID FRACTION

6.1. Results

The results for the superfluid fraction are described in detail elsewhere[2] and only a summary will be given here. The second-sound velocities u_{20} compiled in Appendix A were converted to superfluid fraction (ρ_s/ρ) by the use of Eq. 2. The entropy was taken from Refs. 22 and 66. The heat

capacity was taken from Ref. 34. A comparison was also done using the heat capacity measurements of Refs. 67 and 68 (see Ref. 2). The resulting values of (ρ_s/ρ) are listed in Appendix B.

The errors in the measurement of ρ_s/ρ result from a combination of effects. The fit used to find u_{20} results in errors that are generally quite small. These errors in u_{20} can be converted into errors in ρ_s/ρ by the use of Eq. (2). Furthermore, there is an error in ρ_s/ρ that is associated with an error in the measurement of temperature (Sec. II). These two sources are combined in the usual fashion to give the errors listed in Appendix B. Note that the accuracy with which we know ρ_s/ρ is limited by the accuracy to which we know the cell length (0.1%), and therefore u_{20}, to about 0.2%.

6.2. Comparison with Theory

The expression for the superfluid fraction can be written in the form[69]

$$\frac{\rho_s}{\rho} = k_0(1 + k_1 t)\, t^{\zeta}(1 + D_\rho t^{\Delta}). \tag{17}$$

Here the leading singularity has the exponent ζ, which is predicted to be the same as the exponent ν of the order-parameter correlation length.[70] The best theoretical values for this exponent are from RG calculations done in $d = 3$. They predict $\nu = 0.669 \pm 0.002$ (Ref. 71) and $\nu = 0.672 \pm 0.002$ (Ref. 72). A more recent prediction from an expansion in $\varepsilon = 4 - d$ gave $\nu = 0.671 \pm 0.005$ (Ref. 73). The singular correction term is predicted to have an exponent Δ very near to 0.5.[71,72,74] Previous experimental data[1] are consistent with this prediction. Especially near vapor pressure, where D_ρ is quite small (≈ 0.3), Eq. (17) is quite insensitive to the small differences in the theoretical predictions of Δ, and the value $\Delta = 0.5$ is always used. The amplitude k_1 accounts for any regular dependence of the superfluid fraction on temperature as well as for correction terms of order $t^{2\Delta}$, and should therefore be of order 1. At vapor pressure the effect of this higher order correction can be shown to be negligible[69] for $t < 10^{-3}$, however, neither the *regular* dependence on T, nor the first confluent singular term can be ignored for $t > 10^{-3}$.

The deviations from a best fit to the current data set are shown in Fig. 17. On the ordinate is plotted

$$100 \times \left(\frac{\dfrac{\rho_s}{\rho} - \dfrac{\rho_s}{\rho}(t)}{\dfrac{\rho_s}{\rho}(t)} \right) \tag{18}$$

where $(\rho_s/\rho)(t)$ is the best fit function Eq. (17) and (ρ_s/ρ) are the measured values. In order to obtain the best fit function, a fit is first performed to the data at $t > 10^{-5}$. This fit is used to determine the parameters k_1 and D_ρ. This is allowed since the corresponding terms are known to be inconsequential for $t < 10^{-5}$, and it is desirable because a fit over the entire range is affected by the small but systematic deviations of the data from the best fit function. The remaining parameters, ζ and k_0, are then determined by a fit over the entire data set, with D_ρ and k_1 held constant. The values obtained for the parameters in Eq. (17) were

$$\zeta = 0.6705 \pm 0.0006, \tag{19}$$

$$k_0 = 2.380 \pm 0.015, \tag{20}$$

$$k_1 = -1.74 \pm 0.20, \tag{21}$$

$$D_\rho = 0.396 \pm 0.035. \tag{22}$$

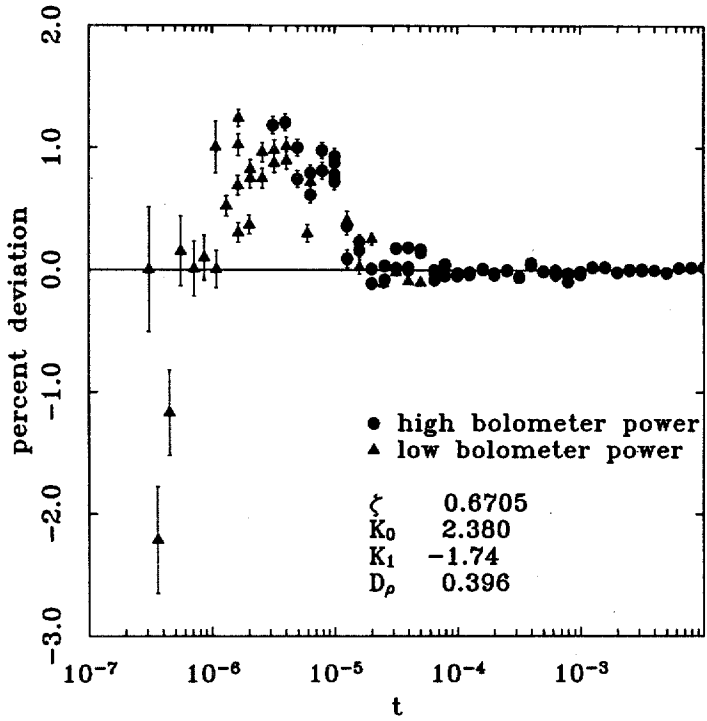

Fig. 17. The percent deviation of the superfluid fraction data from a best fit to Eq. 17. The fitting procedure is described in the text.

This is in excellent agreement with the most recent analysis[75] of the data of Greywall and Ahlers,[1] and also of the most recent analysis[76] of the data of Marek, Lipa, and Phillips.[77] The value for ζ is also in excellent agreement with the theory, which gives values between 0.669 and 0.672 (see above).

Clearly, there is a region inside of $t = 10^{-5}$ where the theoretical form of ρ_s/ρ does not fit the data well. The reasons for this discrepancy are not clear. As discussed extensively above, a thorough search for amplitude and pulse width dependency of the data was carried out. In addition to this, the fit shown in Fig. 17 was repeated for only the smallest amplitude pulses and again for only the shortest length pulses. In either case, the results were unchanged.

Any effect due to a heat flux in the helium (Sec. 3) would tend to decrease u_{20} and therefore ρ_s/ρ; although the data do seem to fall very near T_λ, the rise just inside of $t = 10^{-5}$ appears to be the dominant effect. The effect of gravity, were it sufficiently large, would also cause an apparent decrease in the data for small t; however the expected effect of gravity in the experiment is negligible (Sec. 3).

Although the data closest in have a reduced temperature determined to a precision of ± 5 nK, the accuracy was ± 20 nK, and the effect of shifting T_λ by this amount is shown in Ref. 2. Although neither the fitting parameters nor the goodness of the fit are significantly changed by this procedure, it is clear that the apparent decrease in the fit residuals at $t < 10^{-6}$ may well be an artifact of a small error in T_λ. Deviations in the residuals persist if T_λ is shifted, however the sign of the residuals closest to T_λ may change. Attempts to fit the data with a variable T_λ resulted in a shift in T_λ that was well outside the possible error in our measurement, without a substantial improvement of the fit.

6.3. Comparison with Previous Data

Considerable effort has gone into measuring ρ_s/ρ by a variety of means. Most of the previous measurements were reviewed in Refs. 1 and 78. For work close to T_λ, the measurement of u_2 (or, more directly, of the resonant frequency of second sound in a cavity)[1,77] has provided the most accurate and complete data.[75,77] The results of Greywall and Ahlers are in good agreement with Eqs. 19–22 above. The most recent analysis[76] of the work of Marek, Lipa and Philips[77] also gives a leading exponent ζ that is in good agreement with the results presented here.

7. LARGE AMPLITUDE SECOND SOUND

So far in this study, care has been taken to work in a regime where a lowest-order nonlinear description of the hydrodynamics is sufficient. The situation is quite different if one works outside of this weakly nonlinear regime. In the course of this study, large shocks were observed for $2 \times 10^{-7} < t < 5 \times 10^{-5}$. To our knowledge, these are the first observations of large amplitude second-sound shock waves so near to T_λ.

Some examples of increasingly large amplitude pulses are shown in Figs. 18 to 24. Figure 18 shows the first arrival of five different second-sound pulses at the bolometer at $t = 4.9 \times 10^{-6}$. As usual, this plot shows the bolometer temperature as a function of time, and the temperature amplitudes are therefore twice as large as the amplitude of the disturbance that propagates away into the helium. The input waveform at the heater was a single cycle of a 3600 Hz voltage haversine; only the amplitude

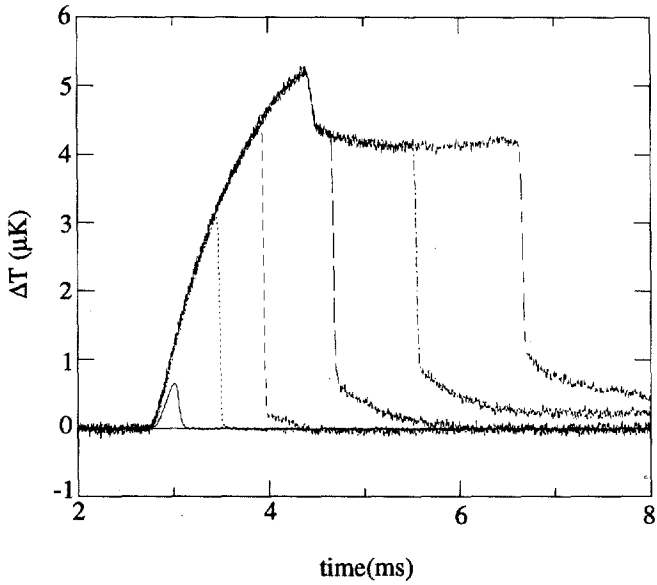

Fig. 18. Example of a series of increasingly larger amplitude pulses at $t = 4.9 \times 10^{-6}$. The first arrivals of the pulses at the bolometer are shown. A single cycle of voltage haversine, $\nu = 3600$ Hz, was applied at the heater. The peak heat flux was: solid line, 0.0582 mW/cm^2; dotted line, 0.633 mW/cm^2; short-dashed line, 1.57 mW/cm^2; long-dashed line, 3.45 mW/cm^2; dot-dashed line, 5.38 mW/cm^2; long-short dashed line, 7.77 mW/cm^2.

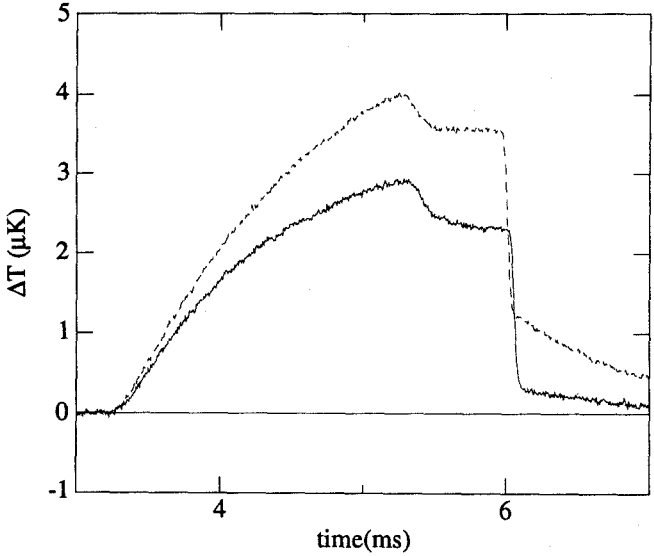

Fig. 19. The effect of different bolometer power levels is demonstrated. Here $t = 3.1 \times 10^{-6}$, and the maximum heat flux of the heater pulse was 1.95 mW/cm^2 ($\nu = 2432$ Hz). Solid line, bolometer power 0.043 μW; dashed line, bolometer power 0.51 μW.

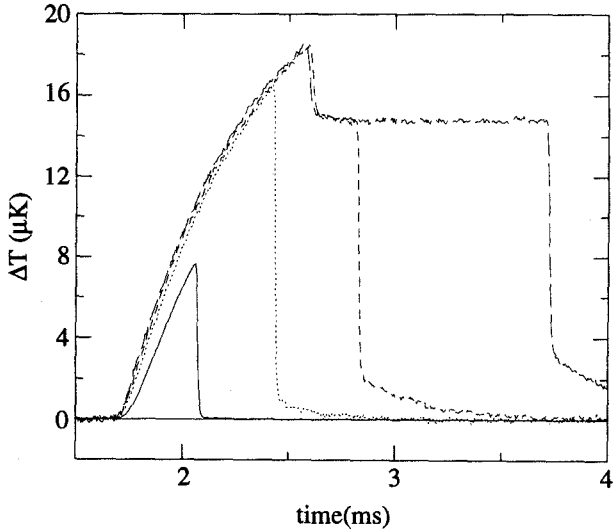

Fig. 20. Large amplitude pulses at $t = 2.0 \times 10^{-5}$. A single cycle of voltage haversine, $\nu = 2387$ Hz, was applied at the heater. The peak heat flux applied was: solid line, 0.810 mW/cm^2; dotted line, 4.01 mW/cm^2; short-dashed line, 8.12 mW/cm^2; long-dashed line, 15.6 mW/cm^2.

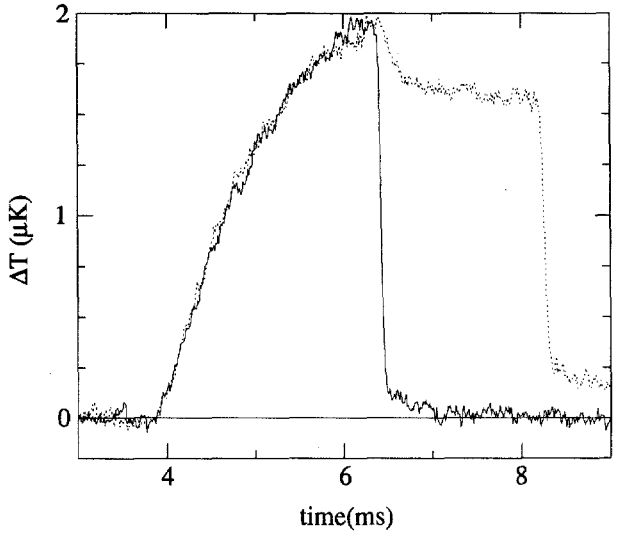

Fig. 21. Large amplitude data for $t = 2.1 \times 10^{-6}$. The heater pulse ($v = 2387$ Hz) had a peak heat flux of: solid line, 0.205 mW/cm^2; dotted line, 0.406 mW/cm^2.

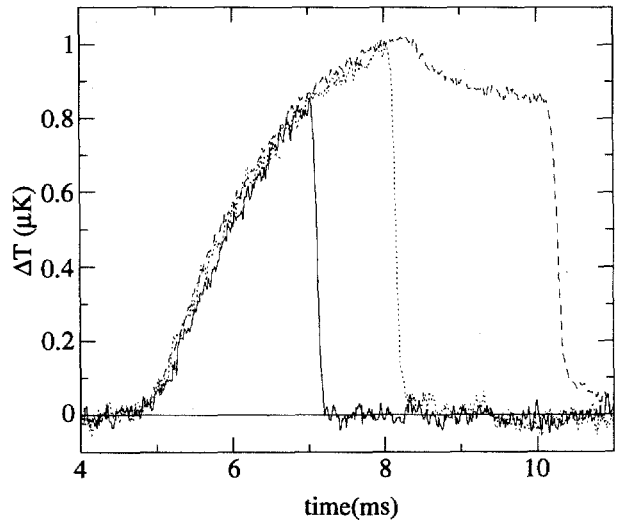

Fig. 22. Large amplitude data for $t = 1.1 \times 10^{-6}$. The heater pulse ($v = 800$ Hz) had a peak heat flux of: solid line, 0.0833 mW/cm^2; dotted line, 0.164 mW/cm^2; short-dashed line 0.328 mW/cm^2.

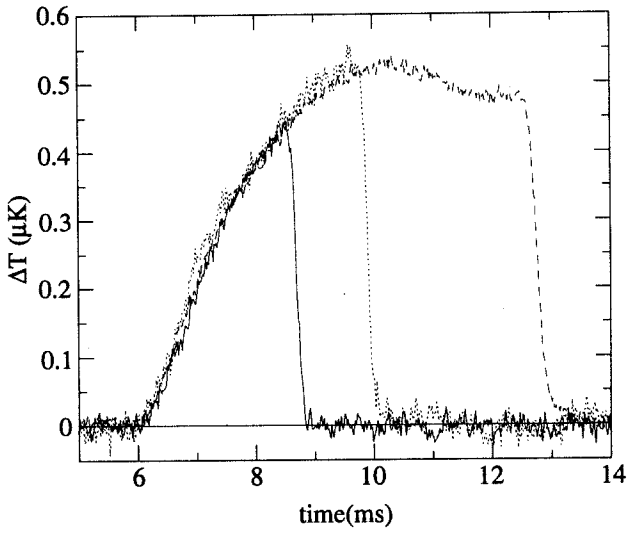

Fig. 23. Large amplitude data for $t = 5.6 \times 10^{-7}$. The heater pulse ($\nu = 623$ Hz) had a peak heat flux of: solid line, 0.0333 mW/cm^2; dotted line, 0.0667 mW/cm^2; short-dashed line 0.133 mW/cm^2.

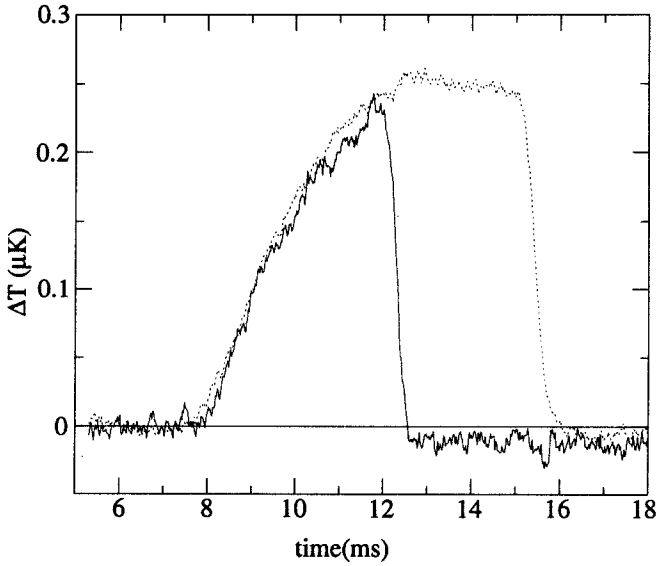

Fig. 24. Large amplitude data for $t = 2.7 \times 10^{-7}$. The heater pulse ($\nu = 447$ Hz) had a peak heat flux of: solid line, 0.0196 mW/cm^2; dotted line, 0.0400 mW/cm^2.

of the haversine has been changed. The peak heat flux at the heater, $Q = V^2/(R_h A)$ ranges from 0.0582 mW/cm^2 to 7.77 mW/cm^2. Here A is the area of the heater (10.08 cm^2), R_h the heater resistance (116.7 Ω) and V is the peak voltage measured across the heater. The smallest amplitude pulse shown was typical of the pulses used in the study of critical second sound presented earlier, where the maximum power input was generally an order or magnitude or more smaller than the powers used here.

Several features of the larger pulses are immediately obvious. There is a clear saturation effect, so that there is a maximum temperature amplitude to the second-sound pulses that is well below $T_\lambda \times t$ ($T_\lambda = 2.172$ K). As the amplitude of the input pulses grows, this maximum is reached, and beyond that a sudden "step" and "shelf" appear in the waveform (alternately, an early "overshoot" develops). A shock still exists, but can no longer be described by Burgers' equation. Beyond the shock, an increasingly large "tail" develops as we increase the amplitude of the haversine.

The tail and quantitative behavior of these pulses depends quite strongly on the power dissipated at the detector. An example of this dependence is shown in Fig. 19. Here $t = 3.1 \times 10^{-6}$, and the heater pulse applied was identical in the two cases. Again the first arrival of the pulses at the bolometer is shown. The only difference between these two pulses was the bolometer power. The pulse with the smaller tail, and also smaller amplitude, was taken with a bolometer power of 0.043 μW, more than ten times smaller than the pulse with the larger tail. Figure 18 was taken at the higher bolometer power (0.51 μW); Figs. 20–24 are all taken at the lower.

Further examples are shown in Figs. 20–24, for $2 \times 10^{-7} < t < 2 \times 10^{-5}$. Large pulses were studied as far out as 5×10^{-5}, and were qualitatively similar to those shown in Fig. 20. As the temperature is increased towards T_λ, the overshoot seems to disappear, but the shelf remains. The tail also seems to *decrease* in size as the λ-point is approached, and in fact a rarefaction becomes evident very near T_λ (Fig. 24). This rarefaction grows beyond the first pulse, and is larger for the successive echoes. Finally, note that, within limits, increasing the pulse length (at sufficiently large amplitude) can have a similar effect as increasing the amplitude.

Effects that are most likely related to those described here have been reported elsewhere in studies done away from T_λ. The amplitude saturation of second-sound shocks has been noted by a number of authors.[4–7, 10, 13–15, 79] Turner[4] discussed in detail the amplitude saturation of second-sound pulses, and interprets them in terms of a "fundamental critical velocity" inherent to the superfluid. Torczynski[5] also discusses this notion in some detail.

For the shock *fronts* discussed in the studies mentioned

above,[4–7, 10, 13–15, 79] the amplitude-saturation is generally followed by a decrease in the shock-amplitude with increasing heater power. Here, we see no decrease in the maximum amplitude of the pulses; however, the shock itself does in fact reach a maximum at a value just before the formation of the "step." Such a "step" in large amplitude pulses has not, to our knowledge, been previously observed; however, Iznankin and Mezhov-Deglin[7] have reported that the decrease in the shock-amplitude with heater power is in fact "jump-like." It is important to note that the previous studies deal primarily with pulses below 1.9 K (where α_2, given by Eq. 3, is positive), and therefore with shock fronts instead of shock tails.

The onset of the warm "tail" noted by Turner has been reported or discussed by a number of other authors.[4, 10, 11, 15, 16] More dramatically, at even larger pulse amplitudes, this "tail" develops into a huge, late, diffusive-looking temperature *overshoot*.[4, 10, 11, 13–16] Similar features were observed in the present data, for the larger bolometer power and inside of 3×10^{-6} in reduced temperature. Many of these effects have recently been described in detail in terms of the dynamics of vortex formation in the superfluid[8–11, 15, 16] and detailed, quantitative studies of the vortex dynamics have been performed.[5–8, 10–16, 80] In particular, the work of Fiszdon, Schwertner, Stamm and Poppe,[16] based on earlier work of Vinen[81] and of Schwarz,[82] has been used in the quantitative analysis of vortex line densities and their effect on large second-sound pulses.[13, 14] Other studies[5–7, 12] have involved the use of successive pulses, where the evaluation of the later pulse depends on the size and length of the first. It has been shown that an initial shock can leave a turbulent trail in its wake that affects the dynamics of a later pulse. In these studies, the vortex tangle left by the initial pulse decays only very slowly compared to the time it takes for the second-sound pulse itself to decay. With this in mind, it is important to note that all of the pulses used in this study were the result of several hundred to several thousand averaged pulses, and that the heater was fired roughly once every other second. Well below T_λ, vortex tangles have been known to persist and affect the dynamics of second-sound pulses for as least 20 seconds after the initial pulse was launched. Recent studies[11, 13, 14, 16] have successfully dealt with just such a problem at temperatures well below the transition. A similar analysis is in order near T_λ.

A variety of boundary-related dissipative effects are also known to exist for very large amplitude pulses. While it seems that most of the noted pulse distortion can be explained in terms of the dynamics of vortex tangles, the mechanism for generating such tangles might, for example, depend on the dynamics of the boundary. Furthermore, effects such as the

temperature rarefaction that develops behind pulses very near T_λ are not obviously attributable to superfluid turbulence. The behavior of the boundary layer at the heater in the presence of large second sound pulses has been discussed by several authors.[4,10,15,79,83–86] A discussion of the nonlinear and critical behavior of the Kaptiza resistance can be found in Refs. 87 and 88.

Finally, while most of the works referenced in this section discuss, in some sense, the breakdown of two fluid hydrodynamics, a series of papers by Atkins and Fox[89–92] explore the nonlinearities inherent in two fluid hydrodynamics that might cause at least some of the effects mentioned above. In particular they explore the nonlinear relationship between heat flux and second-sound amplitude (or shock speed). Although the formation and dynamics of turbulent vortex tangles in the fluid seems the likely cause of many of the observed effects, it is nonetheless necessary to know just how far two fluid hydrodynamics can go in determining the nonlinear behavior of second-sound pulses in order that the onset of superfluid turbulence can be better understood.

In summary, it seems likely that the study of large shocks in the region very near T_λ can provide a detailed probe of the dynamics of the breakdown of superfluidity. The usefulness of second sound as a probe of vortex dynamics has already been demonstrated for the region away from T_λ.[5–8,10–16] Near T_λ, we find qualitatively new phenomena. A more thorough study might also yield information regarding an "intrinsic" critical velocity for He II, or perhaps provide a probe of the ill-understood boundary layer.

8. SUMMARY

We have presented the results of a thorough study of the propagation of nonlinear second sound in the region $2\times10^{-7}<t<10^{-2}$. For second sound with amplitude $\delta t/t<0.1$, the lowest order terms in the two fluid hydrodynamics are found to be sufficient to describe the propagation of second sound. Coupling to first sound and interaction effects can also be ignored in this regime, and the solutions of Burgers' equation describe well the evolution of weakly nonlinear pulses. Using Burgers' equation in a model of second sound propagation, we obtain values for second-sound damping to 3×10^{-7} in reduced temperature, nearly two decades smaller in

reduced temperature than previous measurements. Values for the velocity of second sound are also obtained and from them the superfluid fraction is extracted.

A comparison of theoretical predictions and previous experimental results shows good agrrement of the superfluid fraction data with both. Small but significant deviations from the expected functional form are found very near T_λ, and their origin is not understood. The measured second-sound damping is found to agree well with previous measurements that were performed farther from T_λ. A comparison of D_2 with some current theoretical predictions is also discussed.

Finally, examples of very large amplitude second-sound pulses are shown in the first observation of such pulses near T_λ. A number of new features are observed and suggestions for future work are discussed.

This work was supported by the National Science Foundation through Grants DMR 89-18393 and DMR92-17577.

APPENDIX A. RESULTS FOR D_2 AND u_{20}

Included in this Appendix is the full data set as discussed in Sections 4 and 5. The reduced temperatures are given in the first column. The frequency listed in the second column is the frequency of the haversine used to generate the second-sound pulse in that data set. The initial pulse length is therefore given by u_{20}/v. The errors listed for D_2 are the errors from the fit. For u_{20} the fitting errors underestimate the actual error and so the fitting errors are not listed. The actual error bars correspond to the error in the temperature measurement, which is discussed in detail in the text. $\delta t/t$ is the amplitude of the first pulse echo (used as an initial condition for the fits) expressed as a fraction of the distance to T_λ.

No second-sound damping data was recorded for $t > 5.1 \times 10^{-4}$. In addition, five other damping values are omitted from this set. While second-sound velocities were immune to systematic errors from numerical difficulties in the model, the same was not true of damping. An example is given in Fig. 5, and explained in the accompanying text. Fits exhibiting small but obvious numerical difficulties were omitted from the D_2 data set. Furthermore, occasional drifts in the baseline of the pulse sequence, which were easily spotted by inspection, caused erroneous results for D_2. Such points were also omitted.

10^6 t	ν (Hz)	$10^3\delta t/t$	u_{20} (m/s)	D_2 (10^{-4} cm^2/s)
10051	65475	0.81	7.8710	—
7947.0	59805	1.1	7.1772	—
6310.0	54630	1.5	6.5535	—
5013.0	49853	2.0	5.9833	—
3981.0	45558	2.7	5.4637	—
3161.0	62389	0.89	4.9887	—
3161.0	62389	3.5	4.9890	—
3161.0	41593	0.92	4.9887	—
3161.0	41593	3.6	4.9889	—
2511.0	56989	4.7	4.5567	—
2511.0	26321	5.0	4.5566	—
2511.0	26321	2.5	4.5565	—
1995.0	52048	3.2	4.1625	—
1995.0	34698	3.3	4.1625	—
1584.0	47569	4.4	3.8036	—
1584.0	31713	4.6	3.8035	—
1258.0	43484	5.8	3.4761	—
1258.0	28989	6.0	3.4761	—
1000.2	63570	7.4	3.1781	—
1000.2	39731	8.0	3.1783	—
1000.2	26488	8.3	3.1785	—
794.70	58140	9.8	2.9065	—
794.70	36338	10	2..9057	—
794.70	36338	11	2.9065	—
794.70	24225	11	2.9067	—
631.20	53146	6.7	2.6590	—
631.20	53146	13	2.6586	—
631.20	33216	7.4	2.6589	—
631.20	33216	14	2.6587	—
631.20	22144	7.5	2.6590	—
631.20	22144	15	2.6589	—
500.86	48676	4.5	2.4319	3.66 ± 0.03
500.86	30423	4.9	2.4319	3.87 ± 0.03
500.86	15212	5.2	2.4319	3.75 ± 0.03
397.93	34836	2.9	2.2265	3.82 ± 0.05
397.93	34836	1.5	2.2265	3.83 ± 0.07
397.93	27819	6.5	2.2266	3.93 ± 0.04
397.93	27819	3.1	2.2266	4.18 ± 0.06
397.93	13909	7.0	2.2267	3.98 ± 0.04
397.93	13909	3.1	2.2266	4.14 ± 0.08
319.10	40748	7.8	2.0447	4.03 ± 0.05
319.10	25468	8.7	2.0447	4.08 ± 0.05

10^6 t	ν (Hz)	$10^3\delta t/t$	u_{20} (m/s)	D_2 (10^{-4} cm^2/s)
319.10	25468	17	2.0447	—
319.10	16978	9.0	2.0447	4.32 ± 0.05
319.10	16978	18	2.0447	—
254.07	62210	8.0	1.8746	4.38 ± 0.06
254.07	37326	10	1.8745	4.57 ± 0.06
254.07	23329	12	1.8746	4.59 ± 0.06
254.07	15553	12	1.8746	4.56 ± 0.05
200.03	21368	6.0	1.7109	4.59 ± 0.05
200.03	12368	3.1	1.7109	4.58 ± 0.08
200.03	10684	7.8	1.7109	4.63 ± 0.04
200.03	10684	3.9	1.7110	4.57 ± 0.03
161.42	52193	13	1.5772	4.88 ± 0.07
161.42	19573	20	1.5772	5.02 ± 0.07
161.42	13048	22	1.5773	—
125.97	34836	4.9	1.4353	5.13 ± 0.06
125.97	17971	6.5	1.4355	5.12 ± 0.08
125.97	8971	7.1	1.4355	4.96 ± 0.05
100.04	16443	8.5	1.3155	5.47 ± 0.06
100.04	8222	9.6	1.3156	5.56 ± 0.04
100.02	32886	6.3	1.3154	5.61 ± 0.08
79.322	7235	6.4	1.2052	5.90 ± 0.07
79.305	15070	5.7	1.2056	5.81 ± 0.11
79.305	15070	22	1.2056	6.00 ± 0.09
64.917	13820	7.2	1.1179	6.19 ± 0.09
64.917	6336	8.3	1.1174	5.94 ± 0.08
64.842	13820	27	1.1173	6.25 ± 0.10
50.150	6336	12	1.0154	6.75 ± 0.06
50.141	12672	9.8	1.0154	6.66 ± 0.06
50.141	12672	35	1.0152	7.05 ± 0.07
50.027	12672	7.9	1.0131	6.74 ± 0.72
39.859	11620	10	0.93049	7.05 ± 0.92
39.848	11620	42	0.93168	7.37 ± 0.09
39.830	5809	13	0.93066	7.35 ± 0.09
39.804	11620	11	0.93054	7.02 ± 0.13
31.608	10644	15	0.85366	7.88 ± 0.11
31.602	7096	17	0.85428	7.69 ± 0.08
31.535	10644	14	0.85278	7.94 ± 0.10
25.517	6500	22	0.78818	8.17 ± 0.11
25.508	9750	18	0.78763	8.34 ± 0.09
25.040	9750	17	0.78209	8.46 ± 0.11
20.011	8975	19	0.72075	8.42 ± 0.12
19.987	5983	29	0.71911	8.87 ± 0.13

10^6 t	ν (Hz)	$10^3\delta t/t$	u_{20} (m/s)	D_2 (10^{-4} cm^2/s)
19.945	8975	24	0.71898	8.95 ± 0.09
15.880	8275	11	0.66061	9.88 ± 0.19
15.835	5490	36	0.66038	9.73 ± 0.13
15.827	13180	22	0.66048	9.33 ± 0.10
12.640	7575	27	0.60718	10.28 ± 0.12
12.614	7575	12	0.60767	10.19 ± 0.30
12.579	12120	19	0.60691	10.22 ± 0.17
9.965	10000	18	0.55816	11.01 ± 0.14
9.965	4633	32	0.55830	11.02 ± 0.11
9.958	1853	46	0.55759	11.88 ± 0.20
9.946	10000	18	0.55750	10.94 ± 0.14
7.918	1703	46	0.51249	11.96 ± 0.17
7.898	3917	35	0.51243	11.98 ± 0.09
6.348	3917	12	0.47211	14.31 ± 0.36
6.335	3917	31	0.47192	12.76 ± 0.16
6.334	1567	44	0.47148	12.75 ± 0.18
5.970	3600	24	0.46057	12.41 ± 0.32
4.967	3600	29	0.43188	14.22 ± 0.19
4.963	1440	42	0.43120	13.54 ± 0.21
4.037	3030	23	0.39993	15.13 ± 0.38
4.034	1323	33	0.40006	14.13 ± 0.61
3.950	1323	45	0.39736	15.61 ± 0.19
3.216	2432	29	0.36802	18.11 ± 0.77
3.209	1216	36	0.36753	14.74 ± 0.63
3.125	1216	50	0.36453	15.70 ± 0.24
2.566	1118	36	0.33871	17.42 ± 0.71
2.565	2236	29	0.33830	16.95 ± 0.65
2.048	1028	38	0.31161	20.47 ± 0.61
2.046	2048	47	0.31138	18.79 ± 0.69
2.011	1028	63	0.30884	—
1.640	3780	33	0.28786	21.50 ± 1.2
1.633	945	64	0.28607	18.22 ± 0.76
1.633	945	34	0.28710	21.65 ± 0.95
1.624	1890	52	0.28604	22.40 ± 0.67
1.307	869	36	0.26397	27.57 ± 0.79
1.084	800	61	0.24590	22.82 ± 0.94
1.070	800	17	0.24596	—
0.8640	736	66	0.22647	23.94 ± 0.82
0.7130	677	58	0.21105	28.19 ± 1.0
0.5560	623	64	0.19291	36.17 ± 1.0
0.4510	573	57	0.17758	27.55 ± 0.97
0.3620	527	58	0.16308	41.11 ± 1.4
0.3070	485	57	0.15533	31.03 ± 1.0

APPENDIX B. SUPERFLUID FRACTION RESULTS

The superfluid fraction results and the estimated error for these results are presented below. All parameters are dimensionless. The errors listed are a combination of temperature and fitting errors as discussed in Sec. 6. The accuracy of these measurements is limited by the accuracy to which we know the cell length to 0.2%, however this does not take into account the accuracy to which the heat capacity, C_p, and entropy, σ, are known.

10^6 t	$10^3\rho_s/\rho$	$10^6\delta(\rho_s/\rho)$
0.307	0.10226	0.52
0.362	0.11168	0.50
0.451	0.13080	0.46
0.556	0.15253	0.43
0.713	0.17996	0.41
0.864	0.20489	0.38
1.07	0.23862	0.50
1.084	0.23833	0.37
1.307	0.27159	0.23
1.624	0.31470	0.25
1.633	0.31692	0.28
1.633	0.31466	0.25
1.640	0.31851	0.21
2.011	0.36206	0.27
2.046	0.36766	0.30
2.048	0.36816	0.28
2.565	0.42785	0.35
2.566	0.42888	0.34
3.125	0.49058	0.33
3.209	0.49785	0.38
3.216	0.49911	0.42
3.950	0.57420	0.39
4.034	0.58125	0.44
4.037	0.58086	0.42
4.963	0.66618	0.45
4.967	0.66824	0.45
5.970	0.75077	0.53
6.334	0.78364	0.53
6.335	0.78510	0.53
6.348	0.78563	0.56
7.898	0.91199	0.61
7.918	0.91203	0.61
9.946	1.0625	0.71
9.958	1.0628	0.71
9.965	1.0649	0.71
9.965	1.0654	0.71
12.579	1.2375	0.92
12.614	1.2416	0.93
12.640	1.2395	0.91
15.827	1.4434	0.85
15.835	1.4429	0.85
15.880	1.4436	0.86
19.945	1.6820	0.78
19.987	1.6824	0.79

10^6 t	$10^3\rho_s/\rho$	$10^6\delta(\rho_s/\rho)$
20.011	1.6899	0.79
25.040	1.9573	0.73
25.508	1.9824	0.73
25.517	1.9851	0.73
31.535	2.2873	0.68
31.602	2.2950	0.68
31.608	2.2916	0.68
39.804	2.6756	0.64
39.830	2.6761	0.63
39.848	2.6818	0.63
39.859	2.6750	0.63
50.027	3.1157	0.59
50.141	3.1282	0.58
50.141	3.1290	0.59
50.150	3.1291	0.58
64.842	3.7121	0.54
64.917	3.7156	0.55
64.917	3.7126	0.54
79.305	4.2525	0.51
79.305	4.2527	0.55
79.322	4.2494	0.51
100.02	4.9663	0.49
100.04	4.9678	0.46
100.04	4.9667	0.47
125.97	5.8009	0.46
125.97	5.8008	0.44
125.97	5.7998	0.45
161.42	6.8553	0.42
161.42	6.8557	0.41
161.42	6.8559	0.40
200.03	7.9171	0.37
200.03	7.9163	0.38
200.03	7.9160	0.39
200.03	7.9163	0.37
254.07	9.3020	0.35
254.07	9.3020	0.36
254.07	9.3016	0.38
254.07	9.3021	0.39
319.10	10.838	0.33
319.10	10.839	034
319.10	10.839	0.36
319.10	10.839	0.34
319.10	10.839	0.33
397.93	12.589	0.43

10^6 t	$10^3\rho_s/\rho$	$10^6\delta(\rho_s/\rho)$
397.93	12.588	0.38
397.93	12.590	0.36
397.93	12.590	0.36
397.93	12.590	0.33
397.93	12.591	0.31
500.86	14.693	0.30
500.86	14.692	0.30
500.86	14.693	0.29
631.20	17.167	8.5
631.20	17.169	8.5
631.20	17.172	8.4
631.20	17.172	8.5
631.20	17.172	8.5
631.20	17.173	8.5
794.70	20.055	7.8
794.70	20.052	7.8
794.70	20.052	7.8
794.70	20.041	7.8
1000.2	23.420	7.3
1000.2	23.423	7.3
1000.2	23.425	7.3
1258	27.357	6.8
1258	27.358	6.8
1584	31.965	6.3
1584	31.963	6.3
1995	37.339	5.8
1995	37.340	5.8
2511	43.630	5.4
2511	43.629	5.4
2511	43.627	5.4
3161	50.971	5.1
3161	50.970	5.1
3161	50.975	5.0
3161	50.977	5.0
3981	59.570	4.7
5013	69.593	4.4
6310	81.320	4.1
7947	95.005	3.8
10051	111.273	3.9

REFERENCES

1. D. S. Greywall and G. Ahlers, *Phys. Rev. Lett.* **28**, 1251 (1972); *Phys. Rev. A* **7**, 2145 (1973).
2. L. S. Goldner and G. Ahlers, *Phys. Rev. B* **45**, 13129 (1992).
3. L. S. Goldner, G. Ahlers, and R. Mehrota, *Phys. Rev. B* **43**, 12861 (1991).
4. T. N. Turner, *Phys. Fluids* **26**, 3227 (1983).
5. J. R. Torczynski, *Phys. Fluids* **27**, 2636 (1984).
6. S. K. Nemirovskii and A. N. Tsoi, *Pis'ma Zh. Eksp. Teor. Fiz.* **35**, 229 (1982) [*JETP Lett.* **35**, 286 (1982)].
7. A. Yu. Iznankin and L. P. Mezhov-Deglin, *Zh. Eksp. Teor. Fiz.* **84**, 1378 (1983) [*Sov. Phys. JETP* **57**, 801 (1983)].
8. S. K. Nemirovskii and V. V. Lebedev, *Zh. Eksp. Teor. Fiz.* **84**, 1729 (1983) [*Sov. Phys. JETP* **57**, 1009 (1983)].
9. S. K. Nemirovskii, *Zh. Eksp. Teor. Fiz.* **91**, 1363 (1986) [*Sov. Phys. JETP* **64**, 803 (1986)].
10. S. K. Nemirovskii and A. N. Tsoi, *Cryogenics* **29**, 985 (1989).
11. W. Fiszdon and M. v. Schwerdtner, *J. Low Temp. Phys.* **75**, 253 (1989).
12. M. v. Schwerdtner, G. Stamm, and D. W. Schmidt, *Phys. Rev. Lett.* **63**, 39 (1989).
13. M. v. Schwerdtner, G. Stamm, and W. Fiszdon, *Adv. in Cryogenic Eng.* **35**, 141 (1990). Also presented at *The Third Soviet-German Symposium on Cryogenics*, October 1989.
14. G. Stamm, M. v. Schwerdtner, and W. Fiszdon, *Adv. in Cryogenic Eng.* **35**, 103 (1990). Also presented at *The Third Soviet-German Symposium on Cryogenics*, October 1989.
15. S. K. Nemirovskii and D. W. Schmidt, Max-Planck-Institut für Strömungsforschung Bericht 8/1990 (Göttingen preprint).
16. W. Fiszdon, M. v. Schwerdtner, G. Stamm, and W. Poppe, *J. Fluid Mech.* **212**, 663 (1989).
17. L. S. Goldner, Ph.D. Thesis, University of California at Santa Barbara, Santa Barbara CA 93106 (USA), 1991.
18. W. Y. Tam and G. Ahlers, *Phys. Rev. B* **32**, 5932 (1985).
19. L. E. de Long, O. G. Symko, and J. C. Wheatley, *Rev. Sci. Instrum.* **42**, 147 (1971).
20. L. S. Goldner, N. Mulders, and G. Ahlers, in *Temperature: Its Measurement and Control in Science and Industry*, Edited by J. F. Schooley, Vol. 6 (American Institute of Physics, New York, 1992).
21. American Magnetics, P.O. Box 2509, 112 Flint Road, Oak Ridge, TN.
22. A. Singsaas and G. Ahlers, *Phys. Rev. B* **29**, 4951 (1984).
23. G. C. Straty and E. D. Adams, *Rev. Sci. Instrum.* **40**, 1393 (1969).
24. H. Kierstead, *Phys. Rev.* **153**, 258 (1967).
25. G. Ahlers, *Phys. Rev.* **171**, 275 (1968).
26. G. Ahlers, *J. Low Temp. Phys.* **7**, 361 (1972).
27. United States Department of the Interior, Bureau of Mines, Helium Operations, 1100 So. Fillmore, Amarillo, Texas 79101.
28. S. Kitabatake and Y. Sawada, *J. Phys. Soc. Japan* **45**, 345 (1978).
29. V. Steinberg, private communication.
30. S. K. Nemirovskii, as quoted in M. O. Lutset, S. K. Nemirovskii, and A. N. Tsoi, *Zh. Eksp. Teor. Fiz.* **81**, 249 (1981) [*Sov. Phys. JETP* **54**, 127 (1981)].
31. I. M. Khalatnikov, *An Introduction to the Theory of Superfluidity* (Benjamin, N.Y., 1965).
32. R. A. Fisher, G. E. Brodale, E. W. Hornung, and W. F. Giauque, *Rev. Sci. Instrum.* **39**, 108 (1968).
33. Private communication from Corning Glass Works, Corning, N.Y., 14830.
34. G. Ahlers, in *The Physics of Liquid and Solid Helium*, edited by K. H. Bennemann and J. B. Ketterson (Wiley, NY, 1976), Part I, Ch. 2.
35. S. J. Putterman, *Superfliud Hydrodynamics* (American Elsevier, New York, 1974).
36. G. Ahlers, *Phys. Rev. A* **8**, 530 (1973).
37. S. Putterman and S. Garrett, *J. Low Temp. Phys.* **27**, 543 (1977).
38. Unlike the pulse amplitudes, pulse lengths always refer to the length, from start to finish, of the pulse launched at the heater. This length is equal to u_{20}/ν, where ν is the frequency

of the haversine used to generate the pulse. This is an easily defined length, unlike any length that can be derived from the first pulse echo at the bolometer.
39. Since the data points do not coincide for the two pulses, a cubic spline was used to interpolate between the points of the second pulse.
40. H. J. Mikeska, *Phys. Rev.* **179**, 166 (1969).
41. R. Haussmann, *J. Low Temp. Phys.* **88**, 249 (1992).
42. The area of the bolometer is taken to be 0.0645 cm^2, the area of the square that confines it.
43. L. Kramer, *Phys. Rev.* **179**, 149 (1969).
44. V. L. Ginzburg and A. A. Sobyanin, *Usp. Fiz. Nauk.* **120**, 153 (1976) [*Sov. Phys. Usp.* **19**, 773 (1976)].
45. V. L. Ginzburg and A. A. Sobyanin, *Phys. Lett.* **69A**, 417 (1979).
46. V. L. Ginzburg and A. A. Sobyanin, *J. Low Temp. Phys.* **49**, 507 (1982).
47. In order to account for the round trip travel time of the pulse, Eq. (7) was used to determine the travel times of the pulse towards the bolometer (with the counterflow) and away from the bolometer (against the counterflow). The total travel time was of course the sum of the two, and the velocity in a heat current was extracted from this. It turns out that the term linear in w is quite small and the difference in travel times is therefore inconsequential.
48. G. Ahlers, *J. Low Temp. Phys.* **84**, 173 (1991).
49. G. Ahlers, *Phys. Rev. Lett.* **43**, 1417 (1979).
50. M. J. Crooks and B. J. Robinson, *Phys. Rev. B* **27**, 5433 (1983).
51. R. Mehrotra and G. Ahlers, *Phys. Rev. B* **30**, 5116 (1984); *Phys. Rev. Lett.* **51**, 2116 (1983).
52. B. I. Halperin, P. C. Hohenberg, and E. D. Siggia, *Phys. Rev. B* **13**, 1299 (1976).
53. Note, however, that this model excludes the coupling to first sound, and that more recently, Pankert and Dohm[54] have proposed an extension of model F that includes this coupling.
54. J. Pankert and V. Dohm, *Europhys. Lett.* **2**, 775 (1986); *Phys. Rev. B* **40**, 10842 (1989); *Phys. Rev. B* **40**, 10856 (1989).
55. V. Dohm, *Phys. Rev. B* **44**, 2697 (1991).
56. V. Dohm, *Z. Phys. B* **61**, 193 (1985).
57. R. Schloms and V. Dohm, *Nucl. Phys.* **B328**, 639 (1989).
58. W. Y. Tam and G. Ahlers, *Phys. Rev. B* **33**, 183 (1986).
59. W. Y. Tam and G. Ahlers, *Phys. Rev. B* **37**, 7898 (1988).
60. V. Dohm and R. Folk, *Phys. Rev. Lett.* **46**, 349 (1981).
61. V. Dohm and R. Folk, *Z. Phys. B* **41**, 251 (1981).
62. V. Dohm and R. Schloms, manuscript in preparation.
63. V. Dohm, private communication.
64. This can be calculated from information provided in Ref. 58.
65. V. Dohm, *Z. Phys. B* **60**, 61 (1985).
66. To find σ, the contribution $\Delta\sigma = \int_{T_0}^{T_\lambda} (C_p/T)\, dT$ is subtracted from the value of the entropy at T_λ.
67. J. A. Lipa and T. C. P. Chui, *Phys. Rev. Lett.* **51**, 2291 (1983).
68. The formula used for C_p and best fit values of the partameters were provided in a private communication from J. A. Lipa and T. C. P. Chui, October 1985.
69. G. Ahlers, in *Phase Transitions*, edited by M. Levy, J.-C. Le Guillou, and J. Zinn-Justin (Plenum, NY, 1982), p. 1.
70. B. D. Josephson, *Phys. Lett.* **21**, 608 (1966).
71. J. C. Le Guillou and J. Zinn-Justin, *Phys. Rev. B* **21**, 3976 (1980).
72. D. Z. Albert, *Phys. Rev. B* **25**, 4810 (1982).
73. J. C. LeGuillou and J. Zinn-Justin, *J. Phys. Lett. (Paris)* **46**, L-137 (1985).
74. F. J. Wegner, *Phys. Rev. B* **5**, 4529 (1972).
75. A. Singsaas and G. Ahlers, *Phys. Rev. B* **30**, 5103 (1984).
76. D. R. Swanson, T. C. P. Chui, and J. A. Lipa, preprint.
77. D. Marek, J. A. Lipa, and D. Philips, *Phys. Rev. B* **38**, 4465 (1988).

78. W. Y. Tam and G. Ahlers, *J. Low Temp. Phys.* **66**, 173 (1987).
79. J. C. Cummings, D. W. Schmidt, and W. J. Wagner, *Phys. Fluids* **21**, 713 (1978).
80. H. Liepmann and G. Laguna, *Annu. Rev. Fluid Mech.* **16**, 139 (1984).
81. V. F. Vinen, *Proc. Roy. Soc. Lond. A* **242**, 493 (1957).
82. K. W. Schwarz, *Phys. Rev. B* **38**, 2398 (1988).
83. A. I. Gulyaev, *Pis'ma Zh. Eksp. Teor. Fiz.* **11**, 332 (1970) [*JETP Lett.* **11**, 221 (1970)].
84. A. I. Gulyaev, *Zh. Eksp. Teor. Fiz.* **57**, 59 (1969) [*Sov. Phys. JETP* **30**, 34 (1970)].
85. T. N. Turner, *Physica* **107B**, 701 (1981).
86. A. Yu. Iznankin and L. P. Mezhov-Deglin, *Proceedings of the 17th International Conference on Low Temperature Physics*, edited by U. Eckern, A. Schmid, W. Weber, and H. Wuhl (North Holland, Amsterdam, 1984), p. 71.
87. R. V. Duncan, G. Ahlers, and V. Steinberg, *Phys. Rev. Lett.* **58**, 377 (1987).
88. R. V. Duncan and G. Ahlers, *Jpn. J. Appl. Suppl.* **26-3**, 363 (1987).
89. R. J. Atkins and N. Fox, *J. Phys. C* **20**, 1937 (1987).
90. R. J. Atkins and N. Fox, *J. Phys. C* **19**, 6963 (1986).
91. R. J. Atkins and N. Fox, *J. Phys. C* **17**, 1191 (1984).
92. R. J. Atkins and N. Fox, *J. Phys. C* **16**, 1615 (1983).